The Astrophysical Journal Supplement Series, 282:19 (24pp), 2026 January https://doi.org/10.3847/1538-4365/ae0928

The ALPINE-CRISTAL-JWST Survey: JWST/IFU Optical Observations for 18 Main-sequence Galaxies at $z = 4$–6

A. L. Faisst[1], S. Fujimoto[2,3], A. Tsujita[4], W. Wang[1], N. Nezhad[5], F. Loiacono[6], H. Übler[7], M. Béthermin[8], P. Cassata[9,10], M. Dessauges-Zavadsky[11], R. Herrera-Camus[12,13], D. Schaerer[11], J. D. Silverman[14,15,16,17], L. Yan[18], M. Aravena[13,19], I. De Looze[20], N. M. Förster Schreiber[7], J. González-López[21,22], J. Spilker[23], K. Tadaki[24], C. M. Casey[2,25,26], M. Franco[27], S. Harish[28], H. J. McCracken[29], J. S. Kartaltepe[28], A. M. Koekemoer[30], A. A. Khostovan[28,31], D. Liu[32], J. Rhodes[33], B. E. Robertson[34], R. Amorin[35,36], R. J. Assef[19], A. J. Battisti[37,38,39], J. E. Birkin[23], M. Boquien[40], E. Da Cunha[37,39], P. Dam[9], R. L. Davies[41], D. A. Gómez-Espinoza[42], A. Ferrara[43], Y. Fudamoto[44], S. Gillman[26,45], M. Ginolfi[46,47], G. Gozaliasl[48,49], C. Gruppioni[6], A. Hadi[5], N. Hathi[30], E. Ibar[13,42], R. Ikeda[4,50], H. Inami[51], G. C. Jones[52,53], M. Kohandel[43], Y. Li[23], Y.-H. Lin[1], Z. Liu[14,15,16,27], L.-J. Liu[54], A. S. Long[55], G. Magdis[26,45,56], C. Maraston[57], C. L. Martin[25], I. Mitsuhashi[58], B. Mobasher[5], J. Molina[13,42], A. Nanni[59,60], M. Palla[6,61], A. Pallottini[62], F. Pozzi[6,61], M. Relano[63,64], W. Ren[14,65], D. A. Riechers[66], M. Romano[10,67], D. B. Sanders[68], P. Sawant[59], M. Shuntov[26,56,69], R. Smit[70], L. Sommovigo[71], M. Talia[6,61], L. Vallini[6], E. Veraldi[72], D. Vergani[6], A. P. Vijayan[73], V. Villanueva[12], and G. Zamorani[6]

[1] Caltech/IPAC, 1200 E. California Boulevard, Pasadena, CA 91125, USA; afaisst@caltech.edu
[2] Department of Astronomy, The University of Texas at Austin, Austin, TX 78712, USA
[3] David A. Dunlap Department of Astronomy and Astrophysics, University of Toronto, 50 St. George Street, Toronto, Ontario, M5S 3H4, Canada
[4] Department of Astronomy, School of Science, SOKENDAI (The Graduate University for Advanced Studies), 2-21-1 Osawa, Mitaka, Tokyo 181-8588, Japan
[5] Department of Physics and Astronomy, University of California, Riverside, 900 University Avenue, Riverside, CA 92521, USA
[6] INAF - Osservatorio di Astrofisica e Scienza dello Spazio di Bologna, Via Gobetti 93/3, 40129 Bologna, Italy
[7] Max-Planck-Institute für extratarrestrische Physik, Giessenbachstrasse 1, 85748 Garching, Germany
[8] Université de Strasbourg, CNRS, Observatoire astronomique de Strasbourg, UMR 7550, 67000 Strasbourg, France
[9] Dipartimento di Fisica e Astronomia Galileo Galilei Università degli Studi di Padova, Vicolo dell'Osservatorio 3, 35122 Padova, Italy
[10] INAF—Osservatorio Astronomico di Padova, Vicolo dell'Osservatorio 5, I-35122, Padova, Italy
[11] Observatoire de Genève, Université de Genève, Chemin Pegasi 51, 1290 Versoix, Switzerland
[12] Departamento de Astronomía, Universidad de Concepción, Barrio Universitario, Concepción, Chile
[13] Millenium Nucleus for Galaxies (MINGAL), Av. Ejército 441, Santiago 8370191, Chile
[14] Kavli Institute for the Physics and Mathematics of the Universe (Kavli IPMU, WPI), UTIAS, Tokyo Institutes for Advanced Study, University of Tokyo, Chiba, 277-8583, Japan
[15] Department of Astronomy, School of Science, The University of Tokyo, 7-3-1 Hongo, Bunkyo, Tokyo 113-0033, Japan
[16] Center for Data-Driven Discovery, Kavli IPMU (WPI), UTIAS, The University of Tokyo, Kashiwa, Chiba 277-8583, Japan
[17] Center for Astrophysical Sciences, Department of Physics & Astronomy, Johns Hopkins University, Baltimore, MD 21218, USA
[18] Caltech Optical Observatories, California Institute of Technology, Pasadena, CA 91125, USA
[19] Instituto de Estudios Astrofísicos, Facultad de Ingeniería y Ciencias, Universidad Diego Portales, Av. Ejército Libertador 441, Santiago 8370191, Chile
[20] Sterrenkundig Observatorium, Ghent University, Krijgslaan 281 - S9, B-9000 Gent, Belgium
[21] Instituto de Astrofísica, Facultad de Física, Pontificia Universidad Católica de Chile, Santiago 7820436, Chile 3 Las Campanas, Chile
[22] Observatory, Carnegie Institution of Washington, Raú Bitrán 1200, La Serena, Chile
[23] Department of Physics and Astronomy and George P. and Cynthia Woods Mitchell Institute for Fundamental Physics and Astronomy, Texas A&M University, 4242, USA
[24] Faculty of Engineering, Hokkai-Gakuen University, Toyohira-ku, Sapporo 062-8605, Japan
[25] Department of Physics, University of California, Santa Barbara, Santa Barbara, CA 93109, USA
[26] Cosmic Dawn Center (DAWN), Copenhagen, Denmark
[27] Université Paris-Saclay, Université Paris Cité, CEA, CNRS, AIM, 91191 Gif-sur-Yvette, France
[28] Laboratory for Multiwavelength Astrophysics, School of Physics and Astronomy, Rochester Institute of Technology, 84 Lomb Memorial Drive, Rochester, NY 14623, USA
[29] Institut d'Astrophysique de Paris, UMR 7095, CNRS, and Sorbonne Université, 98 bis boulevard Arago, F-75014 Paris, France
[30] Space Telescope Science Institute, 3700 San Martin Drive, Baltimore, MD 21218, USA
[31] Department of Physics and Astronomy, University of Kentucky, 505 Rose Street, Lexington, KY 40506, USA
[32] Purple Mountain Observatory, Chinese Academy of Sciences, 10 Yuanhua Road, Nanjing 210023, People's Republic of China
[33] Jet Propulsion Laboratory, California Institute of Technology, 4800 Oak Grove Drive, Pasadena, CA 91001, USA
[34] Department of Astronomy and Astrophysics, University of California, Santa Cruz, 1156 High Street, Santa Cruz, CA 95064, USA
[35] Instituto de Investigaciòn Multidisciplinar en Ciencia y Tecnología, Universidad de La Serena, Raúl Bitrán 1305, La Serena, Chile
[36] Departamento de Astronomía, Universidad de La Serena, Av. Juan Cisternas 1200 Norte, La Serena, Chile
[37] International Centre for Radio Astronomy Research (ICRAR), The University of Western Australia, M468, 35 Stirling Highway, Crawley, WA 6009, Australia
[38] Research School of Astronomy and Astrophysics, Australian National University, Cotter Road, Weston Creek, ACT 2611, Australia
[39] ARC Center of Excellence for All Sky Astrophysics in 3 Dimensions (ASTRO 3D), Australia
[40] Université Côte d'Azur, Observatoire de la Côte d'Azur, CNRS, Laboratoire Lagrange, 06000, Nice, France
[41] Centre for Astrophysics and Supercomputing, Swinburne University of Technology, Hawthorn, Victoria 3122, Australia
[42] Instituto de Física y Astronomía, Universidad de Valparaíso, Avda. Gran Bretaña 1111, Valparaíso, Chile
[43] Scuola Normale Superiore, Piazza dei Cavalieri 7, I-56126 Pisa, Italy
[44] Center for Frontier Science, Chiba University, 1-33 Yayoi-cho, Inage-ku, Chiba 263-8522, Japan
[45] DTU-Space, Technical University of Denmark, Elektrovej 327, DK-2800 Kgs. Lyngby, Denmark
[46] Università di Firenze, Dipartimento di Fisica e Astronomia, via G. Sansone 1, 50019 Sesto Fiorentino, Florence, Italy
[47] INAF—Arcetri Astrophysical Observatory, Largo E. Fermi 5, I-50125, Florence, Italy
[48] Department of Computer Science, Aalto University, P.O. Box 15400, FI-00076 Espoo, Finland
[49] Department of Physics, University of Helsinki, P.O. Box 64, FI-00014 Helsinki, Finland

[50] National Astronomical Observatory of Japan, 2-21-1 Osawa, Mitaka, Tokyo 181-8588, Japan
[51] Hiroshima Astrophysical Science Center, Hiroshima University, 1-3-1 Kagamiyama, Higashi-Hiroshima, Hiroshima 739-8526, Japan
[52] Kavli Institute for Cosmology, University of Cambridge, Madingley Road, Cambridge CB3 0HA, UK
[53] Cavendish Laboratory, University of Cambridge, 19 JJ Thomson Avenue, Cambridge CB3 0HE, UK
[54] Physics Department, California Institute of Technology, 1200 E. California Boulevard, Pasadena, CA 91125, USA
[55] Department of Astronomy, The University of Washington, Seattle, WA 98195, USA
[56] Niels Bohr Institute, University of Copenhagen, Jagtvej 128, DK-2200, Copenhagen, Denmark
[57] Institute of Cosmology and Gravitation, University of Portsmouth, Dennis Sciama Building, Burnaby Road, Portsmouth, PO1 3FX, UK
[58] Department for Astrophysical & Planetary Science, University of Colorado, Boulder, CO 80309, USA
[59] National Centre for Nuclear Research, ul. Pasteura 7, 02-093 Warsaw, Poland
[60] INAF—Osservatorio astronomico d'Abruzzo, Via Maggini SNC, 64100, Teramo, Italy
[61] Dipartimento di Fisica e Astronomia "Augusto Righi," Alma Mater Studiorum, Universiá di Bologna, Via Gobetti 93/2, 40129 Bologna, Italy
[62] Dipartimento di Fisica "Enrico Fermi", Universitá di Pisa, Largo Bruno Pontecorvo 3, Pisa I-56127, Italy
[63] Dept. Física Teórica y del Cosmos, Campus de Fuentenueva, Edificio Mecenas, Universidad de Granada, E-18071, Granada, Spain
[64] Instituto Universitario Carlos I de Física Teórica y Computacional, Universidad de Granada, 18071, Granada, Spain
[65] School of Astronomy and Space Science, University of Science and Technology of China, Hefei 230026, People's Republic of China
[66] Institut für Astrophysik, Universität zu Köln, Zülpicher Straße 77, D-50937 Köln, Germany
[67] Max-Planck-Institut für Radioastronomie, Auf dem Hügel 69, 53121 Bonn, Germany
[68] Institute for Astronomy, University of Hawaii, 2680 Woodlawn Drive, Honolulu, HI 96822, USA
[69] University of Geneva, 24 rue du Général-Dufour, 1211 Genève 4, Switzerland
[70] Astrophysics Research Institute, Liverpool John Moores University, 146 Brownlow Hill, Liverpool L3 5RF, UK
[71] Center for Computational Astrophysics, Flatiron Institute, 162 5th Avenue, New York, NY 10010, USA
[72] Scuola Internazionale Superiore Studi Avanzati (SISSA), Physics Area, Via Bonomea 265, 34136 Trieste, Italy
[73] Astronomy Centre, University of Sussex, Falmer, Brighton BN1 9QH, UK
Received 2025 July 3; revised 2025 August 21; accepted 2025 September 8; published 2026 January 6

Abstract

To fully characterize the formation and evolution of galaxies, we need to observe their stars, gas, and dust on resolved spatial scales. We present the ALPINE-CRISTAL-JWST survey, which combines kiloparsec-resolved imaging and spectroscopy from the Hubble Space Telescope, JWST, and Atacama Large Millimeter/submillimeter Array for 18 representative main-sequence galaxies at $z = 4$–6 and $\log(M_*/M_\odot) > 9.5$ to study their star formation, chemical properties, and extended gas reservoirs. The cospatial measurements resolving the ionized gas, molecular gas, stars, and dust on 1–2 kpc scales make this a unique benchmark sample for the study of galaxy formation and evolution at $z \sim 5$, connecting the Epoch of Reionization with the cosmic noon. In this paper, we outline the survey goals and sample selection, and present a summary of the available data for the 18 galaxies. In addition, we measure spatially integrated quantities (such as global gas metallicity), test different star formation rate indicators, and quantify the presence of Hα halos. Our targeted galaxies are relatively metal rich (10%–70% solar), complementary to JWST samples at lower stellar mass, and there is broad agreement between different star formation indicators. One galaxy has the signature of an active galactic nuclei (AGN) based on its emission-line ratios. Six show broad Hα emission suggesting type 1 AGN candidates. We conclude with an outlook on the exciting science that will be pursued with this unique sample in forthcoming papers.

Unified Astronomy Thesaurus concepts: Galaxy formation (595); Galaxy evolution (594); High-redshift galaxies (734); Interstellar medium (847); Galaxy structure (622); Surveys (1671)

Materials only available in the online version of record: figure set

1. Introduction

A top priority in modern astrophysics is to unveil the details of the formation of galaxies in the early Universe and their evolution to the present time, leading to the local cosmic environment we live in and ultimately our own Milky Way. This includes understanding what sets the star formation efficiency and mass assembly rates, the formation of the most massive and dusty galaxies, the emergence of quiescent galaxies, the contribution of mergers to galaxy growth, the coevolution of black holes and their hosts, and importantly the properties of the first stars (for useful reviews on these topics, see J. Kormendy & L. C. Ho 2013; G. De Lucia et al. 2014; P. Dayal & A. Ferrara 2018; L. J. Tacconi et al. 2020; B. E. Robertson 2022; R. S. Klessen & S. C. O. Glover 2023).

Star-forming galaxies spend most of their life on the galaxy star-forming main sequence, a tight relation between stellar mass and star formation rate (SFR; J. Brinchmann et al. 2004; E. Daddi et al. 2007; K. G. Noeske et al. 2007), which has now been robustly identified through ultraviolet (UV) and far-infrared (far-IR) observations out to $z \sim 5$ in large samples of galaxies (e.g., C. L. Steinhardt et al. 2014; K. I. Caputi et al. 2017; Y. Khusanova et al. 2021; J. Cole & C. Papovich 2023; L. Clarke et al. 2024; J. W. Cole et al. 2025). During that time, the evolution of galaxies is determined by a balance between the consumption or removal of gas through star formation or outflows and the replenishment of gas through accretion or minor mergers onto the galaxy's disk (e.g., R. Davé et al. 2012; S. J. Lilly et al. 2013; R. Feldmann 2015; L. J. Tacconi et al. 2020). Spatially integrated galaxy properties have been measured with large statistical samples across billions of years of galaxy history to understand the evolution of galaxies overall. But we still lack the understanding of the underlying processes that govern the subgalactic spatial scales, especially in galaxies at high redshifts. For example, we do not yet have a

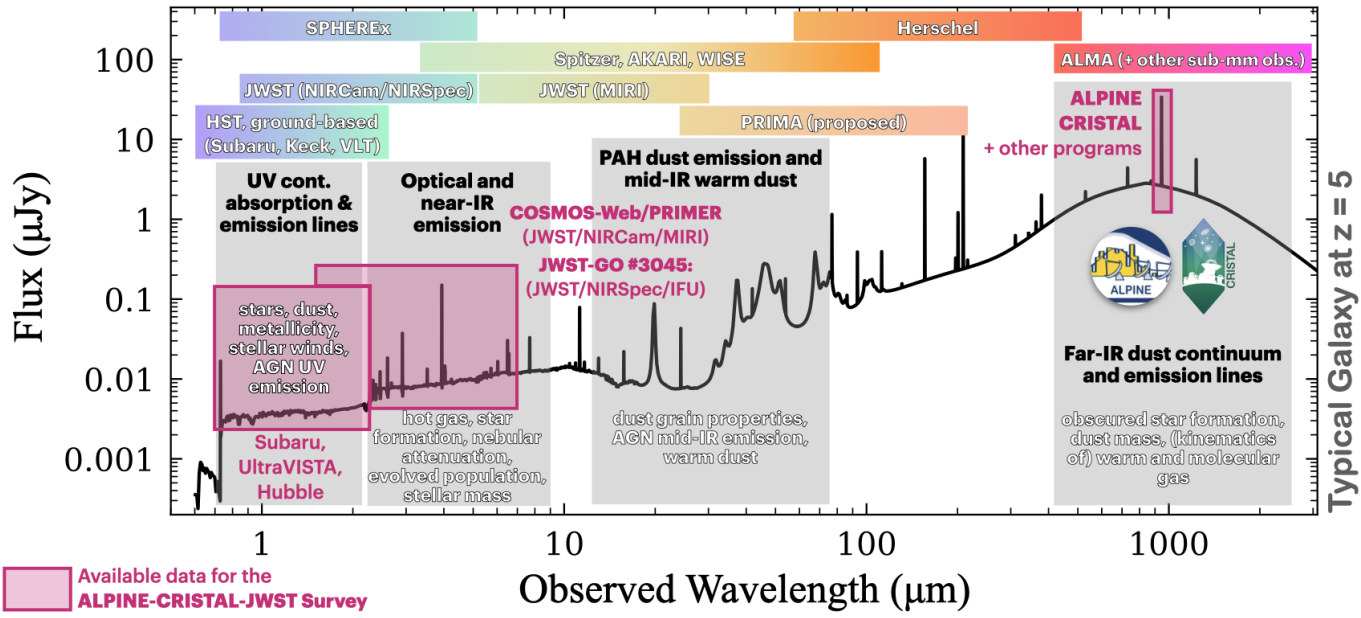

Figure 1. The spectrum of a typical $z = 5$ galaxy overlaid with wavelength regimes of physical interest. A selection of ground- and space-based facilities are highlighted (including past missions like Spitzer and Herschel). The wavelength regions that are observed by the available data of the ALPINE-CRISTAL-JWST survey sample are shown as magenta boxes. We note the lack of observations at mid-IR and far-IR wavelength, covering warm dust emission and polycyclic aromatic hydrocarbons (PAHs), important tracers of the dust grain distribution, at high redshifts. This wavelength range may be filled in by future facilities such as PRIMA (J. Glenn 2025).

consistent picture of the details of metal enrichment and star formation efficiency (e.g., P. Dayal et al. 2013; G. Popping et al. 2017; A. P. Vijayan et al. 2019; H. Katz et al. 2022; C. R. Choban et al. 2024; A. Pallottini et al. 2025), dust distribution (e.g., D. P. Triani et al. 2021; A. Ferrara & C. Peroux 2021; L. Sommovigo et al. 2022; F. Ziparo et al. 2023), origin and impact of outflows (e.g., S. Gallerani et al. 2018; E. Pizzati et al. 2020), or the growth of supermassive black holes and the structure formation in the early Universe (e.g., P. Dayal & A. Ferrara 2018; M. Volonteri et al. 2021). While much progress has been made recently in characterizing galaxies in the Epoch of Reionization (EoR, $z \gtrsim 6$), it is of fundamental importance to study the connection between this primordial epoch and mature galaxies at cosmic noon ($z = 2$–3). Understanding the intertwined connections between these epochs and processes requires the study of baryons (stars, gas, and dust) on galactic scales in the interstellar and circumgalactic medium (ISM and CGM, respectively). With their energy output spanning more than 3 orders of magnitude in wavelength (Figure 1), these processes can only be characterized through a multiwavelength photometric and spectroscopic study using a combination of ground- and space-based observatories.

Prior to the James Webb Space Telescope (JWST), such multiwavelength spectroscopic studies at resolved spatial scales have only been possible for (unlensed) galaxies at cosmic noon and later epochs. One notable example is the Spectroscopic Imaging survey in the Near-infrared with SINFONI (SINS; N. M. Förster Schreiber et al. 2009) and later, in combination with the zCOSMOS survey (S. J. Lilly et al. 2007), the SINS/zC-SINF survey (N. M. Förster Schreiber et al. 2018). These surveys combine ground-based observations from the Very Large Telescopes' (VLT) SINFONI AO-assisted spectrograph in the rest-frame optical, and Hubble Space Telescope (HST) rest-frame UV/optical observations of a large sample of spectroscopically confirmed $z \sim 2$ galaxies. The combination of these instruments enabled breakthroughs in our understanding of the buildup of such galaxies, including the properties of their star-forming clumps, kinematics, and the origin of outflows (e.g., R. Genzel et al. 2011; S. F. Newman et al. 2012; R. L. Davies et al. 2019)—ultimately emphasizing the need of such studies at higher redshifts. Similarly, the SHiZELS survey provided resolved emission-line maps of narrow-band selected galaxies at $z = 0.8$–2.2 with SINFONI-AO (A. M. Swinbank et al. 2012). Significantly larger samples with similar measurements at $0.7 < z < 2.7$ but more statistical power have been realized later by the KMOS^{3D} (N. M. Förster Schreiber et al. 2019; E. Wisnioski et al. 2019) and the KROSS survey (J. P. Stott et al. 2016). In parallel to that, large spectroscopic campaigns such as the MOSFIRE Deep Evolution Field survey (MOSDEF; M. Kriek et al. 2015) or the Keck Baryonic Structure Survey (KBSS; G. C. Rudie et al. 2012; C. C. Steidel et al. 2014) delivered integrated spectroscopic data revealing the evolution of chemical properties at $z < 3$ (e.g., A. L. Strom et al. 2017; R. L. Sanders et al. 2021).

At higher redshifts, such comparable studies have not been possible due to two reasons; the lack of multiwavelength coverage at sufficiently long wavelengths into the IR to probe the rest-frame optical emission lines at $z > 3$ and the lack of sufficient spatial resolving power and/or sensitivity. With JWST up and running, such detailed analyses are now possible for the first time, covering the galaxies' history deep into the EoR. Large photometric and spectroscopic surveys in prominent JWST fields such as JADES (D. J. Eisenstein et al. 2023) and CEERS (S. L. Finkelstein et al. 2025) now provide integrated spectroscopy of galaxies at high redshifts to study their chemical compositions and the abundances of active galactic nuclei (AGN). Designated surveys such as the Chemical Evolution Constrained using Ionized Lines in

Interstellar Aurorae survey (A. L. Strom et al. 2023) or the Assembly of Ultradeep Rest-optical Observations Revealing Astrophysics (AURORA) survey (A. E. Shapley et al. 2025) use the power of deep spectroscopic observations at rest-frame UV and optical wavelengths for detailed studies of chemical and ionization properties of such galaxies.

However, all of these large surveys provide spatially integrated measurements, making it challenging to disentangle the different physical processes defined at smaller spatial scales and to compare the observations at high redshifts to local studies at similar physical scales. Furthermore, complementary observations at rest-frame far-IR wavelengths are necessary to compare the ionized phases with those of cold gas and dust. It is therefore of profound importance to establish a proper, well-studied multiwavelength benchmark sample at $z = 4$–6 between the EoR and cosmic noon to (i) measure the chemical and structural properties of this galaxy population, (ii) define a comparison sample for similar studies at lower and even higher redshifts with future facilities, and (iii) anchor state-of-the-art cosmological simulations.

The Atacama Large Millimeter/submillimeter Array (ALMA) changed the landscape for directly detecting rest-frame far-IR light in high-redshift galaxies. It enabled a first look at rest-frame far-IR wavelengths to constrain the dust content via the far-IR continuum and cold gas properties through the measurement of singly ionized carbon ([C II]) emission at 158 μm for typical main-sequence galaxies at high redshifts (D. A. Riechers et al. 2014; P. L. Capak et al. 2015; T. Hashimoto et al. 2019; S. Carniani et al. 2020; Y. Harikane et al. 2020; Y. H. V. Wong et al. 2022). Prior to ALMA, [C II] had only been observed at high redshifts for single starburst galaxies and not spatially resolved (e.g., D. Iono et al. 2006; R. Maiolino et al. 2009). The ALPINE-ALMA large program (#2017.1.00428.L, PI: Le Fèvre; M. Béthermin et al. 2020; A. L. Faisst et al. 2020; O. Le Fèvre et al. 2020) was the first step toward achieving a multiwavelength post-EoR galaxy sample. ALPINE combined rest-frame UV to optical photometry with ALMA observations of the far-IR dust continuum and [C II] at rest-frame 158 μm for 118 typical post-EoR main-sequence galaxies at $z = 4$–6. ALPINE has led to several breakthroughs in the study of dust, gas, kinematics, and outflows of post-EoR galaxies (see the comprehensive ALPINE review paper by A. L. Faisst et al. 2022). Specifically, it shows that the relation between [C II] and SFR is in place out to $z \sim 5$ (D. Schaerer et al. 2020) and showcases the use of [C II] for inferring the dynamics, molecular gas mass, and depletion times (M. Dessauges-Zavadsky et al. 2020). ALPINE data also suggest that dust and UV emission may be spatially offset, which could lead to significant underestimation of the dust components based on rest-frame UV light only (A. L. Faisst et al. 2017; L. Sommovigo et al. 2022; M. Killi et al. 2024). Furthermore, outflows (which may be related to the creation of [C II] halos) are common in these star-forming high-redshift galaxies (S. Fujimoto et al. 2019; M. Ginolfi et al. 2020; E. Pizzati et al. 2023; J. E. Birkin et al. 2025). But its success also came with new questions about (i) the dust production/destruction in early galaxies, (ii) the details of cold and hot gas kinematics, (iii) the frequency of supermassive black holes (SMBHs) residing in typical high-redshift galaxies, and (iv) the origin of the reported [C II] halos extending out to 10 kpc into the CGM. These are key questions to be answered to understand early galaxy evolution.

To answer these questions, we must go one step further and obtain far-IR observations at higher spatial resolutions and fill in the gap of missing spatial resolved spectroscopy at rest-frame optical wavelengths.

The ALMA-CRISTAL survey (R. Herrera-Camus et al. 2025) achieved the former by providing high-resolution far-IR follow-up observations of 19 ALPINE galaxies, thus enabling the first study of the gas and dust properties of these galaxies on kiloparsec scales.

The aim of this new ALPINE-CRISTAL-JWST survey, of which science goals, data, sample selection, and basic measurements are presented in this paper, is to leverage these excellent data with rest-frame optical spectroscopy. This program uniquely combines the capabilities of JWST NIRSpec/integral field unit (IFU) spatially resolved rest-frame optical spectroscopy with JWST NIRCam imaging, HST rest-frame UV data, and high-resolution ($0\farcs3$) ALMA [C II] and dust continuum observations for a sample of 18 massive ($\log(M_*/M_\odot) > 9.5$) main-sequence galaxies at $z = 4$–6 (Figure 1). This post-EoR multiwavelength photometric and spectroscopic survey establishes a benchmark sample to study in detail early galaxy formation and evolution and to connect the EoR with mature galaxy evolution at cosmic noon.

In this paper we give an overview of the ALPINE-CRISTAL-JWST survey and present a few key results based on spatially integrated measurements. We note that the presentation of the detailed data reduction and resolved measurements is beyond the scope of this paper and would distract from its main purpose to present the general purpose of this survey. Specifically, the details of the data reduction of the JWST/NIRSpec IFU data are presented in S. Fujimoto et al. (2025). In Section 2, we introduce the science goals of the survey and describe the sample selection. In Section 3, we detail the available multiwavelength data. Section 4 includes basic measurements for our sample, which are compared to other observations from the literature at lower and higher redshifts. We conclude in Section 5 with an outlook of upcoming science results from this survey.

Throughout this work, we assume a ΛCDM cosmology with $H_0 = 70\,\mathrm{km\,s^{-1}\,Mpc^{-1}}$, $\Omega_\Lambda = 0.7$, and $\Omega_\mathrm{m} = 0.3$ and magnitudes are given in the AB system (J. B. Oke 1974). We use a Chabrier initial mass function (IMF; G. Chabrier 2003) for stellar masses and SFRs.

All measurements derived work are tabulated in the Appendix A and catalogs containing these data will be accessible to the public upon request. For details on the data reduction of the JWST/NIRSpec IFU observations we refer to the companion paper by S. Fujimoto et al. (2025).

2. The ALPINE-CRISTAL-JWST Survey

2.1. Motivation and Science Goals

A careful study of galaxy evolution and to answer the above questions require the measurement of all baryon components constituting a galaxy (stars, dust, and gas), which is only possible with the combined observations of different telescopes in both imaging and spectroscopic modes across the spectrum (Figure 1).

Although the ALPINE survey provided a valuable multi-wavelength picture of post-EoR galaxies, several key

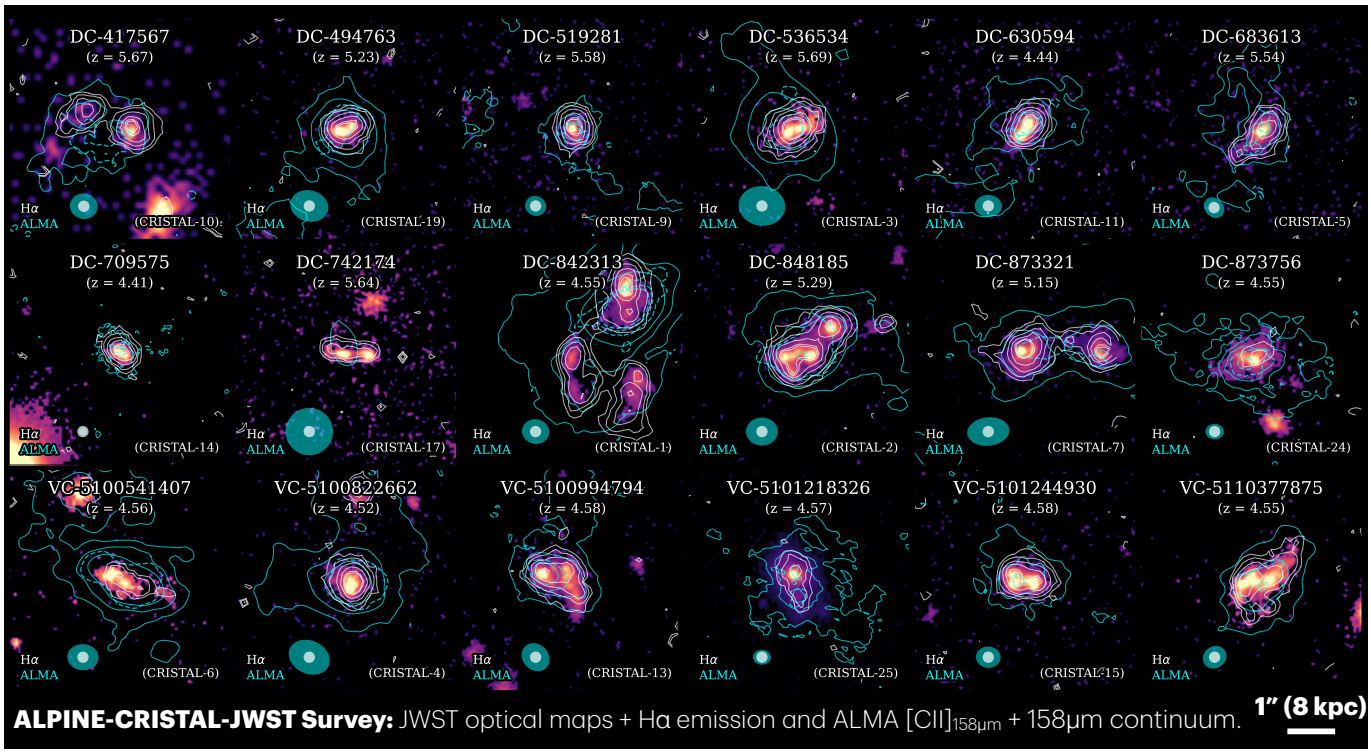

Figure 2. Collage of the 18 targets part of the ALPINE-CRISTAL-JWST sample. For each panel, the background shows the COSMOS-Web JWST/NIRCam F277W image (except for DC-417567 for which we show HST WFC3/F160W). The Hα map from JWST/NIRSpec IFU observations is indicated with the white contours. The CRISTAL ALMA data are shown as cyan contours ([C II]: solid; 158 μm continuum: dashed). The contours show 3σ, 5σ, 10σ, 20σ, 40σ, and 50σ levels for JWST and 3σ, 10σ, and 20σ levels for ALMA data. The ALMA (cyan) and NIRSpec/NIRCam (white) beam/PSF are indicated in all panels.

observations were missing, which led to several fundamental unknowns including ionized gas properties and kinematics, chemical properties such as metal abundance, star formation, and black hole growth. For example, no deep rest-frame optical imaging was available (see A. L. Faisst et al. 2020), ALMA observations were too coarse to identify the finer structure of dust and [C II] emission, and spectroscopy was limited to the rest-frame UV wavelength and lacked spatial resolution (O. Le Fèvre et al. 2013; R. J. Bouwens et al. 2015; G. Hasinger et al. 2018). Observations using the Spitzer Space Telescope made headway to studying the rest-frame optical emission of galaxies (C. L. Steinhardt et al. 2014; K. I. Caputi et al. 2017) and yield the first measurements of Hα emission at $z \sim 5$ including the ALPINE sample (e.g., H. Shim et al. 2011; D. P. Star k et al. 2013; A. L. Faisst et al. 2019), but at a resolution and depth not enough to perform resolved studies or spectroscopy. Similarly, Herschel's sensitivity was only sufficient to detect the mid-/far-IR continuum in stacks of typical main-sequence galaxies at $z > 4$ such as the ALPINE galaxies (e.g., M. Béthermin et al. 2020).

With HST, JWST, and ALMA operating at the same time, it is now finally possible to overcome these limitations and provide a multiwavelength photometric and spectroscopic benchmark sample to study the connection between primordial galaxy formation in the EoR and the galaxy population at cosmic noon. The ALPINE-CRISTAL-JWST survey, presented in this work, combines observations with HST and ALMA with the unprecedented sensitivity and spatial resolution of JWST imaging and integral field spectroscopy for a unique sample of 18 main-sequence galaxies at $z = 4$–6 (Section 2.2). Figure 2 showcases the available data for each of the 18 targets from JWST imaging (background image in NIRCam/F277W), JWST spectroscopy (white contours showing the Hα emission measured by the NIRSpec/IFU), and ALMA (cyan solid and dashed contours for [C II] and dust continuum emission). Current observatories are uniquely suited to provide a comprehensive multiwavelength view of galaxies in the redshift range of $4 < z < 6$. Note that JWST would not cover Hα in galaxies at $z \gtrsim 7$ unless using MIRI (J. A. Zavala et al. 2025), which, however, is significantly less sensitive than NIRSpec. The redshift range $4 < z < 6$ is crucial to understand the connection between primordial galaxy formation in the EoR and late galaxy evolution at cosmic noon. It is the epoch in time where galaxies significantly grow their stellar mass, enrich their ISM and CGM with metals, and establish their structures before they reach the peak of their star formation and eventually become quiescent. Importantly, the results from this program can be compared directly to similar efforts at $z > 6.5$ (REBELS-IFU; R. J. Bouwens et al. 2022; L. E. Rowland et al. 2025) and lower redshifts (e.g., SINS at $z \sim 2$ and others mentioned earlier) to render a complete picture of galaxy evolution. Therefore, the main goal of the ALPINE-CRISTAL-JWST survey is to establish a multiwavelength kiloparsec-resolution post-EoR benchmark sample at the highest redshifts to date to connect early and late galaxies. This survey enables the study of how the first galaxies mature and grow in structure and chemical composition to become the systems we observe at later cosmic times.

The ALPINE-CRISTAL-JWST survey is designed to address the following questions:

1. *How and where are stars being formed?* Constraining the modes of star formation in conjunction with gas and dust abundances and a detailed study of star

formation histories using combined imaging and spectroscopic data.
2. *How is the ISM enriched?* Studying the interplay between star formation, gas, metals, and dust by detailed measurements of (spatially resolved) metal abundances and photoionization properties.
3. *How is dust produced?* Deciphering the dominant modes of dust production and variations in dust content by the combination of chemical and dust evolution models and the spatial distribution of rest-frame UV, optical, and far-IR light.
4. *What is the contribution of AGN to the typical galaxy population?* Understanding the occurrence of AGN in typical main-sequence galaxies via broad optical emission lines and line ratio diagnostics to investigate the coevolution of SMBHs and host galaxies in relation to AGN found by recent JWST surveys.
5. *What is the relation between the ISM and the CGM?* Constraining the baryon cycle and enrichment of the CGM and solving the origin of the [C II] halos by measuring the ionized properties and outflows of the surrounding gas.
6. *How does the kinematics of hot and cold gas compare?* Study the kinematics of the stellar+ionized and gas disk via the velocity fields of Hα and [C II] at redshifts in the midst of cosmic disk formation.

The ALPINE-CRISTAL-JWST survey will answer these questions within a representative sample of main-sequence galaxies at $z = 4$–6 by combining observations from HST, JWST, and ALMA.

2.2. Sample Selection

The ALPINE-CRISTAL-JWST survey consists of 18 galaxies selected from the combined survey data of the larger ALPINE-ALMA program (M. Béthermin et al. 2020; A. L. Faisst et al. 2020; O. Le Fèvre et al. 2020) and the CRISTAL survey (R. Herrera-Camus et al. 2025). ALPINE comprises a set of 118 galaxies selected from the COSMOS (N. Scoville et al. 2007) and GOODS-S (M. Giavalisco et al. 2004) fields with ALMA observations in band 7, targeting [C II] and the rest-frame $\sim$158 μm dust continuum emission. The ALPINE sample was selected by requiring secure spectroscopic redshifts at $z = 4$–6 from Keck/DEIMOS and VLT/VIMOS observations (O. Le Fèvre et al. 2013; G. Hasinger et al. 2018; A. A. Khostovan et al. 2025) with a cut applied in [C II] luminosity based on the $M_{\rm UV}$–$L_{\rm [C\,II]}$ relation derived from the pilot sample by P. L. Capak et al. (2015). The spectroscopic redshifts are derived from Lyα emission as well as UV absorption lines to minimize a sample bias toward strong emission-line galaxies. X-ray or UV line detected AGN are excluded from this sample to focus solely on typical main-sequence galaxies.

The ALPINE-CRISTAL-JWST sample is then constructed from the ALPINE sample with the following requirements:

1. a robust ($>5\sigma$ integrated) [C II] detection,
2. follow-up observations by ALMA of [C II] emission at a spatial resolution of $\sim$0.″3 close to the pixel size of the JWST/NIRSpec IFU optical spectroscopy,
3. imaging observations with JWST/NIRCam at $1 - 5$ μm in at least four bands,
4. coverage with HST in ACS/F814W and at least one redder HST band, and
5. detectability ($>5\sigma$) of all strong optical emission lines (such as Hβ, [O II]$_{3727}$ (unresolved), [O III]$_{5007}$, Hα, [N II]$_{6585}$, and [S II]$_{6718}$) with the JWST/NIRSpec IFU in less than 2 hr on-source time.

To satisfy the requirement of high-resolution [C II] observations, we chose galaxies observed by the ALMA-CRISTAL survey as well as ALMA programs #2022.1.01118.S (PI: Béthermin) and #2019.1.00226.S (PI: Ibar) providing beam sizes on the order of 0.″3. The optical emission-line signal-to-noise ratio (SNR) selection was driven by faint lines such as [N II], [S II], and [O II] whereas the other lines, which are intrinsically brighter, were observed at higher SNR. The disperser/filter combinations G235M/F170LP and G395M/F290LP were used to cover these lines for the redshift range of $z = 4.4$–5.9. The Hα emission-line fluxes to estimate the JWST/NIRSpec exposure times were predicted from the SFRs of the galaxies, which themselves were derived from the combined UV and far-IR emission (D. Schaerer et al. 2020) or SED fitting (A. L. Faisst et al. 2020). The remaining line fluxes were predicted based on their ratios with respect to Hα for conservative assumptions of gas-phase metallicities (derived from the expected mass–metallicity relation; R. Maiolino et al. 2008) and dust obscuration (derived from SED fitting to the COSMOS photometry; A. L. Faisst et al. 2020). The SNRs were estimated using the JWST exposure time calculator `Pandeia` (K. M. Pontoppidan et al. 2016) in the given disperser/filter configurations. Overall, this technique worked well and we achieved the expected SNRs for all galaxies except three. For the latter, we likely underpredicted the dust attenuation, leading to a lower-than-expected SNR in the blue grating.

The final sample consists of 18 galaxies with HST, JWST (imaging and IFU spectroscopy), and 0.″3 beam size ALMA observations. We note that one galaxy (DC-417567/CRISTAL-10) is not covered by JWST photometric observations but has HST ACS/F814W as well as WCF3/F105W, F125W, and F160W data. This galaxy was included in Phase 2 of the JWST proposal process to replace a galaxy with weak [C II] emission suggested by the new CRISTAL observations (see R. Herrera-Camus et al. 2025). We emphasize that no selection is imposed on the far-IR continuum emission measured by ALPINE or CRISTAL. In the final sample, however, 15 out of the 18 galaxy systems are dust continuum detected at $>3\sigma$ (M. Béthermin et al. 2020; R. Herrera-Camus et al. 2025). In this paper, we follow the naming convention of ALPINE, but we list the corresponding CRISTAL names of the targets in Table 1 and Figure 2.

Figure 3 shows the final sample of 18 galaxies on the stellar mass versus SFR plane. In this case, the SFRs are derived from the total UV+far-IR luminosity, or, if no ALMA far-IR continuum is available, from SED fitting (see Section 3.5). The sample is compared to the parent ALPINE sample (white circles) and galaxies selected from the COSMOS2020 (J. R. Weaver et al. 2022) catalog at $z \sim 5$, as well as other JWST-detected sources at $z = 4$–6 (M. Curti et al. 2023; K. Nakajima et al. 2023; T. Morishita et al. 2024; A. Sarkar et al. 2025). Galaxies indicated by filled squares are mergers identified by M. Romano et al. (2021) based on their low-resolution (1″) [C II] kinematic analysis (see also similar analysis by R. Ikeda et al. 2025). This includes the targets

Table 1
Identifications and Available HST and JWST Data for the Targets

Name			z_{opt}	R.A.	Decl.	HST						JWST									
							WFC3					NIRCam								MIRI	
ALPINE	CRISTAL	Others		(J2000)	(J2000)	ACS F814W	F105W	F110W	F125W	F140W	F160W	F090W	F115W	F150W	F200W	F277W	F356W	F410M	F444W	F770W	F1800W
DC-417567[a,b]	C-10	HZ2[c]	5.6700	150.51701	1.92889	×	×		×		×										
DC-494763[b]	C-19	⋯	5.2337	150.02127	2.05338	×	×		×	×	×		×	×		×			×	×	
DC-519281[a,b]	C-09	⋯	5.5759	149.75372	2.09100	×		×			×		×	×		×			×		
DC-536534[a,b]	C-03	HZ1[c]	5.6886	149.97183	2.11818	×	×	×	×		×		×	×		×			×	×	
DC-630594[b]	C-11	⋯	4.4403	150.13583	2.25788	×			×	×	×	×	×	×	×	×	×	×	×	×	
DC-683613[a,b]	C-05	HZ3[c]	5.5420	150.03926	2.33718	×	×		×		×		×	×		×			×	×	×
DC-709575[b]	C-14	⋯	4.4121	149.94610	2.37579	×					×		×	×		×			×		
DC-742174[b]	C-17	⋯	5.6360	150.16302	2.42560	×			×	×	×	×	×	×	×	×	×	×	×	×	
DC-842313[b]	C-01	⋯	4.5537	150.22721	2.57638	×	×		×	×	×		×	×		×			×		
DC-848185[a,b,e]	C-02	HZ6[c]/ LBG-1[d]	5.2931	150.08963	2.58635	×	×		×		×		×	×		×			×		
DC-873321[a,b]	C-07	HZ8[c]	5.1542	150.01690	2.62661	×	×		×		×		×	×		×			×		
DC-873756[e,f,g]	C-24	⋯	4.5457	150.01132	2.62781	×	×	×	×	×	×		×	×		×			×		
VC-5100541407[b]	C-06	⋯	4.5630	150.25382	1.80935	×		×		×	×		×	×		×			×		
VC-5100822662[b]	C-04	⋯	4.5205	149.74130	2.08094	×		×			×		×	×		×			×		
VC-5100994794[b]	C-13	⋯	4.5802	150.17143	2.28726	×			×	×	×	×	×	×	×	×	×	×	×	×	
VC-5101218326[e,f]	C-25	⋯	4.5739	150.30207	2.31461	×	×				×		×	×		×			×		
VC-5101244930[b]	C-15	⋯	4.5803	150.19856	2.30058	×			×	×	×	×	×	×	×	×	×	×	×	×	
VC-5110377875[h]	⋯	⋯	4.5505	150.38475	2.40842	×					×		×	×		×			×		

Notes. Note that all targets have rest-frame optical IFU spectroscopy from JWST/NIRSpec and 0.″3 resolution ALMA 158 μm continuum and [C II] spectroscopic data. All galaxies are observed by the ALPINE-ALMA program (2017.1.00428.L, PI: Le Fèvre; O. Le Fèvre et al. 2020) and detected in [C II]. Names in bold indicate galaxy systems with additional 150 μm dust continuum detection (M. Béthermin et al. 2020; I. Mitsuhashi et al. 2024).

[a] Type-1 AGN candidate from W. Ren et al. (2025).

[b] Observed by the ALMA-CRISTAL survey (2021.1.00280.L, PI: Herrera-Camus; R. Herrera-Camus et al. 2025).

[c] See P. L. Capak et al. (2015).

[d] See D. A. Riechers et al. (2014).

[e] Band 4 observations available (2024.0.01401.S, PI: Herrera-Camus).

[f] Observed by ALMA program 2019.1.00226.S (PI: Ibar).

[g] Band 9 observations available (2024.0.01401.S, PI: Herrera-Camus).

[h] Observed by ALMA program 2022.1.01118.S (PI: Béthermin).

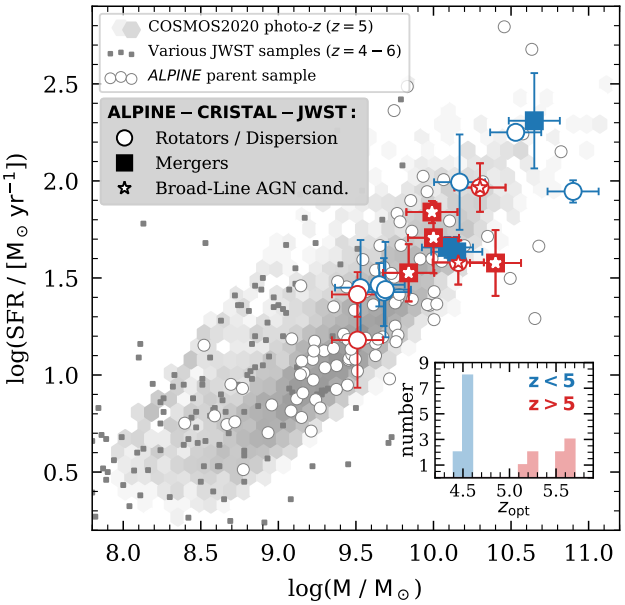

Figure 3. The 18 targets of the ALPINE-CRISTAL-JWST survey on the stellar mass vs. SFR plane. The targets are shown with large symbols, split in $z < 5$ (blue) and $z > 5$ (red) subsamples. The redshift distribution is shown in the inset. Furthermore, we indicate rotators/dispersion-dominated (open circles) and mergers (solid squares) identified by low-resolution $\sim 1''$ [C II] kinematics data (M. Romano et al. 2021). Candidate type 1 (broad-line) AGN are indicated with a star (W. Ren et al. 2025). The ALPINE parent sample is shown as small white circles (A. L. Faisst et al. 2020). In addition, we show galaxies at $z \sim 5$ from the COSMOS2020 catalog (J. R. Weaver et al. 2022) as well as various JWST-detected galaxies at $z = 4$–6 from the literature (small gray squares; see the text for references).

DC-417567, DC-519281, DC-536534, DC-842313, DC-873321, VC-5100541407, and VC-5100822662. However, note that the higher resolution ALMA data from CRISTAL suggest that also DC-683613 (A. Posses et al. 2025) and DC-848185 (R. Davies et al. 2025, in preparation) are likely interacting/merging.

We also indicate type 1 broad-line AGN candidates selected by a rigorous logic involving a comparison between the Bayesian information criteria (BIC) for a fit with and without broad lines and a high SNR broad-line detection (for details, we refer to W. Ren et al. 2025). The Hα broad line widths for the final candidates range from 600 km s^{-1} (least robust candidate) to 2800 km s^{-1} (most robust candidate). This type 1 AGN candidate sample includes the targets DC-417567, DC-519281, DC-536534, DC-683613, DC-848185, and DC-873321. Note that none of the targets, by construction, are specifically identified as AGN based on their X-ray or radio emission. Furthermore, we find that none of our targets (except for DC-873756) lie in the AGN region of the Baldwin–Phillips–Terlevich (BPT) diagram (J. A. Baldwin et al. 1981) derived from the new JWST data presented here (see Section 4).

The redshift distribution of the sample spans the range $z = 4.4$–5.7 with a gap between $z = 4.6$ and 5.1. This gap originates from the original ALPINE selection to avoid a low atmospheric transmission at the observed frequency of [C II]. The sample concentrates at $\log(M/M_\odot) > 9.5$, hence populates the more massive end of the $z \sim 5$ galaxy population but 2 orders of magnitude less massive than the knee of the mass function at $z = 5$ (I. Davidzon et al. 2017). It therefore complements optimally other JWST-detected galaxy samples at lower stellar masses.

3. Multiwavelength Observational Data

In the following sections we provide a summary of the acquisition and reduction of the data for the 18 targets observed by different observatories (Table 1). Details about the observing programs are presented in Table A1. Figure 2 shows a portrait of the available data for all 18 targets in the sample.

3.1. JWST NIRSpec/IFU Observations

The JWST/NIRSpec IFU cycle 2 GO program #3045 (PI: Faisst) builds the backbone of the ALPINE-CRISTAL-JWST survey data. The technical details, especially the details of the data reduction process, of this program are presented in S. Fujimoto et al. (2025). Here, we provide a brief overview of the technical details of the program and the reduction of the NIRSpec/IFU data.

The observations were carried out during cycle 2 between April and May 2024. The targets were observed with the NIRSpec IFU in configurations G235M/F170LP and G395M/F290LP at medium spectral resolution ($R \sim 1000$) to cover all strong optical emission lines. However, target DC-842313 was observed in G395H/F290LP by the cycle 2 program #4265 (PIs González-López & Aravena, see also M. Solimano et al. 2025). These data are also included in this work. For program #3045, the integration times vary from 500 to 7200 s per target per configuration, with a two-point sparse cycling dither pattern. The integration time for program #4265 is 12,000 s, with a nine-point small cycling dither. No off-center background observations or leakage calibration exposures were taken. Instead, the background is measured from background pixels within the $3'' \times 3''$ IFU field of view. The final 3σ flux rms (average over the different targets) of our observations is 6.6×10^{-21} erg s^{-1} cm^{-1} Å^{-1} for G235M and 1.3×10^{-21} erg s^{-1} cm^{-1} Å^{-1} for G395M/G395H (the flux per target varies slightly per target, for details, see S. Fujimoto et al. (2025).

The data were reduced using the STScI pipeline (version 1.16.0) with the CRDS context `jwst_1298.pmap` to a final pixel scale of $0.''1$ px^{-1}. We followed the procedure developed by the ERS TEMPLATES team (#1355; PIs Rigby & Vieira, see also J. E. Birkin et al. 2023; J. Rigby et al. 2023; B. Welch et al. 2023). Several additional steps to improve the final data quality were implemented, including improved background subtraction, stripe removal, and rescaling of the error cubes (S. Fujimoto et al. 2025). The cubes were subsequently astrometrically aligned to the JWST COSMOS-Web images, which are referenced to Gaia DR3 (Gaia Collaboration et al. 2023), see also M. Franco et al. (2025). To this end, first NIRCam F277W and F444W pseudocontinuum images were created by convolving the cubes (pixel by pixel) with the corresponding filter transmission curves. The centroid positions of the collapsed cubes (obtained by a Gaussian fit) are then compared to the corresponding JWST/NIRCam images. We found offsets on the order of $0.''1$–$0.''3$ between the NIRCam image and collapsed cube, which we correct for. These offsets are within the expected pointing uncertainty of JWST. The final astrometric precision is comparable with that of COSMOS-Web (i.e., a few 10 mas). In addition, we checked the absolute and relative calibration of both grism

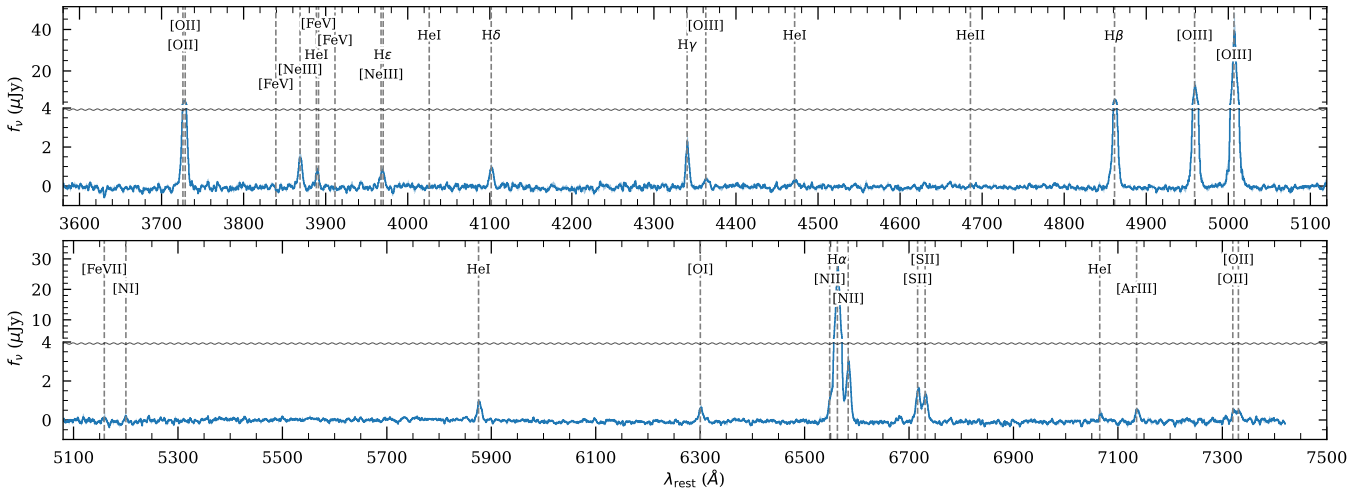

Figure 4. Stacked spectrum of all 18 ALPINE-CRISTAL-JWST survey targets (note that the y-axis is broken at 4 μJy to make the higher fluxes more visible). Some prominent and common emission lines are indicated by the vertical dashed lines. The spectra have been continuum subtracted before stacking. More details on the derivation of the spectra can be found in Section 4.

configurations. This was achieved by convolving the respective spectra (spatially integrated over an aperture of 0.″5 diameter) with the transmission curves of the NIRCam F277W and F444W filters. This synthetic broadband photometry was then compared to the photometry measured on the F277W and F444W COSMOS-Web images in the same aperture. We find that the absolute flux calibration is better than 30% with a 1σ scatter of $\sim$10%. The relative calibration of the two grism configurations is better than 5%.

The stacked and spatially integrated spectrum of all the 18 targets is shown in Figure 4. The spectra of the individual targets are shown in Figure B1 in Appendix B (see Section 4 for details). All the strong optical emission lines are detected as well as some fainter lines such as [Ne III]$_{3868}$, He I (3889 Å, 5875 Å), Hϵ, Hδ, Hγ, [O I]$_{6300}$, [Ar III]$_{7138}$, and auroral oxygen lines ([O III]$_{4363}$ and the [O II]$_{7322,32}$ doublet). These are diagnostic lines sensitive to the ionization parameter (log(U)), gas metallicity, nebular dust attenuation ($E_n(B-V)$), electron density (n_e), and in some cases electron temperatures (T_e), which can be used to derive T_e-based gas-phase metallicities.

3.2. ALMA Submillimeter Observations

All 18 targets are part of the ALPINE survey, a large cycle 5 ALMA program (#2017.1.00428.L, PI: Le Fèvre) targeting the [C II] emission in 118 galaxies at $z = 4$–6. A survey overview is provided by O. Le Fèvre et al. (2020) with the data reduction presented by M. Béthermin et al. (2020). The ancillary data and the measurement of the physical properties of the ALPINE galaxies is described in A. L. Faisst et al. (2020).

The ALPINE-CRISTAL-JWST sample has additional follow-up ALMA observations at $\lesssim$0.″3, to complement the ALPINE-ALMA data at higher spatial resolutions. Out of the 18 targets, 15 have follow-up observations by the ALMA-CRISTAL survey (#2021.1.00280.L, PI: Herrera-Camus, R. Herrera-Camus et al. 2025). The sensitivity achieved by CRISTAL is comparable to ALPINE but at a 3–4 times higher angular resolution and 2–7 times longer integration times. Out of the remaining three galaxies, two (DC-873756 and VC-5101218326) were observed by the program #2019.1.00226.S (PI: Ibar) and one (VC-5110377875) by the program #2022.1.01118.S (PI: Béthermin). For the former, the medium- (0.″3) and high-resolution (0.″15) visibilities were combined. The data from these two additional programs are discussed in more detail in T. Devereaux et al. (2024) and M. Béthermin et al. (2023), respectively. In all these cases, the data are reduced using the standard ALMA reduction pipeline `CASA` (CASA Team et al. 2022), combining the high-resolution data with the lower resolution observations from the ALPINE survey. This combination provides excellent coverage from small compact to more extended diffuse submillimeter emission.

3.3. JWST NIRCam and MIRI Observations

The JWST/NIRCam and MIRI observations provide rest-frame optical imaging at unprecedented resolution. These imaging data are crucial for resolved SED studies (see J. Li et al. 2024).

All except one target are covered by the JWST cycle 1 GO treasury program COSMOS-Web (#1727, PIs: Kartaltepe & Casey; C. M. Casey et al. 2023). This program provides observations in four NIRCam filters (F115W, F150W, F277W, and F444W) and one MIRI filter (F770W). Due to the smaller field of view of MIRI and the adopted survey strategy, only 7 out of the 18 galaxies have MIRI coverage. We use the official data products distributed by the COSMOS-Web team, which include additional updates on background subtraction and artifact removal compared to the standard STScI pipeline. Details of the NIRCam and MIRI data reductions are described by M. Franco et al. (2025) and S. Harish et al. (2025), respectively. A catalog of sources is presented in M. Shuntov et al. (2025). In addition, four galaxies were covered by the JWST cycle 1 GO treasury program PRIMER (#1837, PI: Dunlop, reduced by the COSMOS-Web team) providing (in addition to COSMOS-Web) imaging in the NIRCam filters F090W, F115W, F150W, F200W, F277W, F356W, F444W, and F410M as well as in MIRI F770W and F1800W. All data are aligned to the Gaia astrometric reference frame, consistent with the JWST/NIRCam IFU cubes (Section 3.1).

We refer to Table 1 for a full list of JWST data and to Table A1 for a full list of program numbers. The JWST

imaging data is also shown in Figure B1 in Appendix B for each of our targets.

3.4. Other Ancillary Data and Planned Observations

All targets reside in the COSMOS field (N. Scoville et al. 2007) providing HST/ACS F814W imaging data (A. M. Koekemoer et al. 2007) as well as a wealth of data from ground-based facilities. See J. R. Weaver et al. (2022) for an overview of these data. In addition, the galaxies are covered by several HST WFC3/IR pointings including filters F105W, F110W, F125W, F140W, and F160W. These provide crucial rest-frame UV and optical wavelength coverage offset from the central wavelengths of the JWST filters. The programs are listed in Table A1 and include 3D-HST (G. B. Brammer et al. 2012; I. G. Momcheva et al. 2016), COSMOS-DASH (L. A. Mowla et al. 2019; S. E. Cutler et al. 2022), COSMOS-DASH-3D (L. A. Mowla et al. 2022), and the CANDELS-HST survey (N. A. Grogin et al. 2011; A. M. Koekemoer et al. 2011).

The ALPINE-CRISTAL-JWST survey targets will also be part of several future observations by HST and JWST. Five out of the 18 galaxies will be covered by the ORCHIDS cycle 3 JWST program in NIRSpec/IFU G395H/F290LP (#5974, PI: Aravena) with the goal to understand better the [C II] halos surrounding these galaxies with deep spectroscopy. In total 12 galaxies will be included in the COSMOS-3D cycle 3 JWST/NIRCam (grism) survey (#5893, PI: Kakiichi) providing additional imaging observations in F115W/F200W/F356W (NIRCam) and F1000W/F2100W (MIRI) as well as slitless spectroscopy in F444W. Finally, 17 galaxies will be included in the CLUTCH cycle 32 HST multicycle program (#17802, PI: Kartaltepe), providing deeper ACS/F814W observations together with new ACS/F435W, ACS/F606W, and WFC3/F098W imaging (note that the galaxies will be undetected in the bluer bands provided by CLUTCH due to their high redshifts).

3.5. SED-based Stellar Masses and SFRs

Various physical measurements were inherited from previous works (see Table A2). Specifically, stellar masses and SFRs were derived from SED fitting including the photometry from ground-based observatories and Spitzer from the COSMOS2020 catalog (J. R. Weaver et al. 2022) and JWST imaging from the COSMOS-Web program. Here we adopt the measurements derived using `CIGALE` (D. Burgarella et al. 2005; M. Boquien et al. 2019) and described in detail in I. Mitsuhashi et al. (2024) and R. Herrera-Camus et al. (2025). We note that these results are consistent with J. Li et al. (2024) who measure spatially resolved stellar masses and SFRs using `MAGPHYS` (E. da Cunha et al. 2008; E. da Cunha et al. 2015) including the ALMA continuum data, and N. E. P. Lines et al. (2025) who use `Bagpipes` (A. C. Carnall et al. 2018; A. C. Carnall et al. 2019) not including the ALMA continuum data.

In addition to SED fitting, we computed the SFRs from different observed indicators, spanning star formation timescales from 10 to 100 Myr. These indicators include [C II], Hα, [O II], and the UV+far-IR luminosity. For the [C II]-derived SFRs, we used the parameterization by D. Schaerer et al. (2020; including UV+IR, with $a = 7.37$ and $b = 0.83$). From the dust-corrected Hα and [O II] luminosities, we derived SFRs using the R. C. Kennicutt (1998) parameterizations[74] and the nebular dust attenuation measurements described in Section 4.5. For targets detected in the ALPINE+CRISTAL ALMA continuum, we computed the total SFR measurement based on the sum of the SFRs derived from UV and far-IR continuum (SFR_{UV+IR}). The former is derived from rest-frame UV photometry of HST and ground-based imaging (see A. L. Faisst et al. 2020) and the latter is the total far-IR luminosity derived from the ALMA 158 μm continuum by using the appropriate conversion factors (M. Béthermin et al. 2020; I. Mitsuhashi et al. 2024). In both cases, the luminosity is converted to SFR using the R. C. Kennicutt (1998) parameterizations. Table A2 lists the different SFR measurements. The SFR indicators are compared in Section 4.7.

[74] We correct from a Salpeter to Chabrier IMF by multiplying with a factor of 0.61 (e.g., P. Madau & M. Dickinson 2014).

4. JWST/NIRSpec IFU Measurements

In this section, we outline basic measurements of diagnostic lines and related properties derived from the NIRSpec IFU spectra. We focus here on spatially integrated measurements and emission-line maps. Resolved measurements will be explored in future works.

4.1. Propagation of Measurement Uncertainties

Because there are significant cross correlations and dependencies between the parameters derived in the following, it is not straightforward to propagate uncertainties through these calculations. To provide realistic uncertainties on the following measurements, we therefore adopted an extensive end-to-end Monte Carlo sampling method to properly propagate and estimate the uncertainties of all the quantities reported below. To do so, we created 200 different NIRSpec/IFU cube realizations by perturbing each pixel according to its uncertainty derived from the rescaled IFU error cubes, which include all observational effects and sky background (S. Fujimoto et al. 2025). This method generally works well unless the errors are significantly correlated between the pixels. This is, however, not the case given that the PSF is comparable to the pixel size of the IFU data. Interpixel correlations are neglected here for simplicity. Each of the cube representations is then analyzed end to end, resulting in 200 different measurements. The final measurements are obtained as the medians and their 1σ percentiles.

4.2. Emission-line Maps and Integrated Spectra

We first create spatially integrated spectra for each of the 18 targets from their NIRSpec cubes. For the spatial integration, we define a mask encompassing emission of the sum of the [O II], [O III], Hα, and Hβ line maps. Creating these maps for a given target involves an iterative process: First, we spatially integrated the spectrum in a $1''$ aperture around the target coordinates (center of mass measured on NIRCam images) to derive a first-guess integrated spectrum. From that spectrum we measured the full width at half-maximum (FWHM) of the emission lines (see Section 4.3). We then created maps of each of the emission lines by integrating the cubes across three FWHMs ($\sim 3 \times 340\,\mathrm{km\,s^{-1}}$) along the spectral dimension. To derive the final masks, we stacked these emission-line maps and selected pixels for which the total flux is detected at an SNR > 5. Note that because different emission lines are covered by the two gratings G235M and G395M, we created two such masks for each target. Using those masks, we then derived the spatially integrated spectrum for each grating by

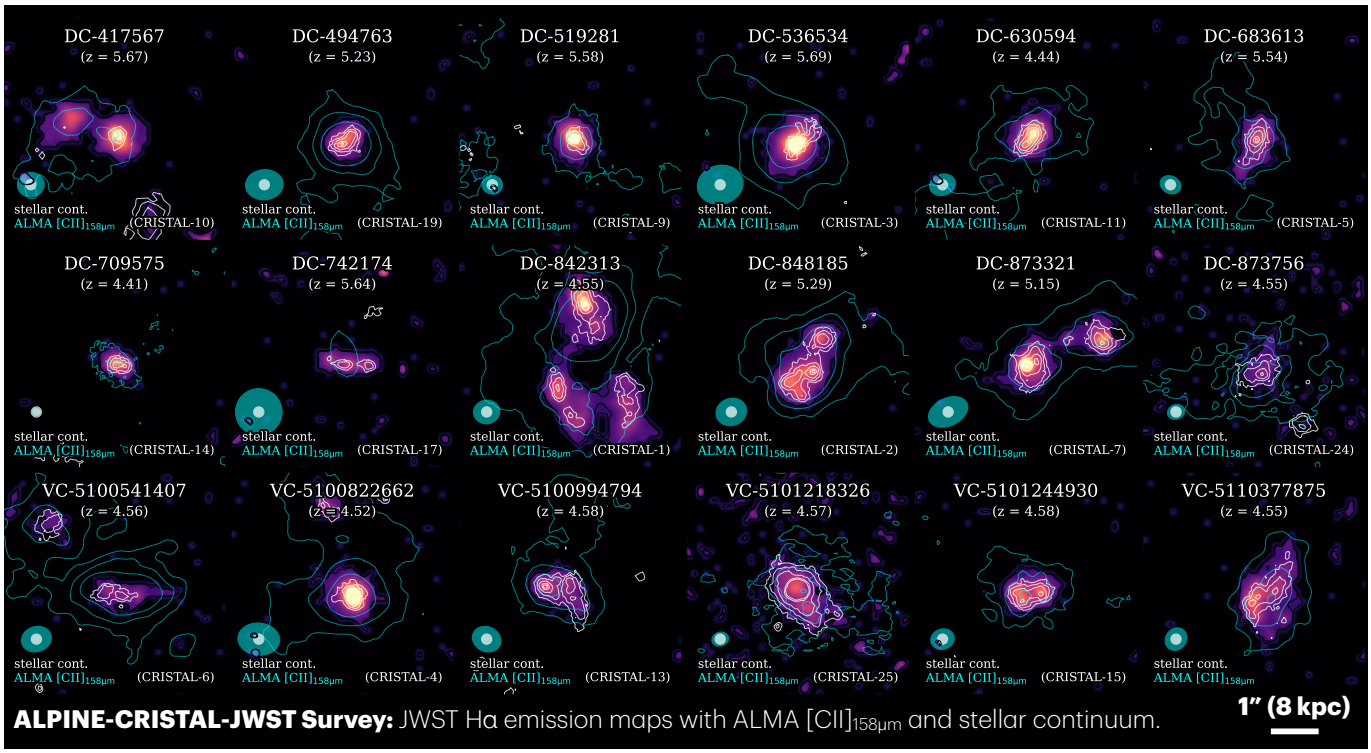

Figure 5. Hα emission-line maps derived from the NIRSpec/IFU observations for the 18 galaxies in the ALPINE-CRISTAL-JWST sample. The line maps are cut off at 5σ. The white contours show the rest-frame optical light (JWST/NIRCam F277W and HST WFC3/F160W for DC-417567) and cyan contours show [C II] emission from the ALMA-CRISTAL program. The contours show 5σ, 10σ, 20σ, 40σ, and 50σ levels for JWST and 3σ, 10σ, and 20σ levels for ALMA data. The ALMA (cyan) and NIRSpec (white) beam/PSF are indicated in all panels.

summing up the spectra in each pixel in the mask. In a final step, the two one-dimensional spectra of the two gratings are combined, using median stacking over the wavelength region where they overlap. We note that generally the SNR ratio is higher in G395M in the overlapping region. Figure 5 shows the Hα maps together with the JWST NIRCam imaging and ALMA data. Figure B1 show the G235M+G395M (or G235M +G395H in the case of DC-842313) combined spectrum as well as emission-line maps for each target individually.

4.3. Emission-line Fitting and Line Diagnostic Diagrams ("BPT diagrams")

Having measured the spatially integrated spectra of each of the targets, we then fit the total fluxes of bright optical lines including some fainter auroral lines. The line measurements are summarized in Table A4 and the process is described below.

We simultaneously fit lines within seven different emission-line complexes: (i) the *spectrally* unresolved [O II]$_{3727}$ doublet; (ii) the [Ne III]$_{3868}$ neon line; (iii) Hγ and the [O III]$_{4363}$ auroral line; (iv) Hβ, [O III]$_{4959}$, and [O III]$_{5007}$; (v) [N II]$_{6548}$, Hα, and [N II]$_{6585}$; (vi) the [S II]$_{6718}$ and [S II]$_{6732}$ doublet; and (vii) the [O II]$_{7322}$ and [O II]$_{7332}$ auroral lines. With this split, we can deblend lines that are close by and at the same time treat the complexes independently to account for changes in the noise and line spread function. The line flux ratios of the [N II] lines are fixed to three (D. E. Osterbrock & G. J. Ferland 2006). We assume the same FWHM for line doublets, however, not for different line species in different line complexes. This is because the line spread function may change across the wavelength range covered by the gratings. Fitting for the FWHM and central wavelengths between different complexes mitigates this effect. In the end, we found that the results are consistent within $\sim$10% in FWHM (except broad lines, see below). Here, we fit each line (except Hα) with a single Gaussian with variable integrated flux, central wavelength, and FWHM (or σ) using the Python `lmfit` package.[75] The continuum is subtracted by masking the line and fitting the first-order polynomial. For Hα we fit a double Gaussian representing a broad and narrow-line component for cases in which the reduced χ^2 is significantly smaller (by a factor of 2, ranging between 0.5 and 2.0) compared to a single Gaussian fit. We found that a double Gaussian is a better fit for 7 out of 18 targets. For four out of these seven targets, the broad component contributes significantly (>30%) to the total Hα flux (see Table A4). These targets are DC-519281, DC-536534, DC-842313, and DC-848185 (shown to have strong outflows by R. Davies et al. (2025, in preparation) and may have a type 1 AGN in the northwest component). All of these were also selected by W. Ren et al. (2025) as type 1 AGN candidates based on their broad Hα lines. For the remaining three targets, the broad Hα line may be dominated by outflows. This will be analyzed in a subsequent paper.

Figure 6 shows the targets on three different line ratio diagnostic diagrams (type 1 AGN candidates from W. Ren et al. 2025 are indicated in gray—only narrow-line flux is considered). On each diagram, we show common separation lines between AGN and star-forming galaxies (L. J. Kewley et al. 2001; G. Kauffmann et al. 2003; L. J. Kewley et al. 2013; G. Mazzolari et al. 2024; B. E. Backhaus et al. 2025; J. Scholtz et al. 2025) as well as measurements from the literature at low

[75] https://lmfit.github.io/lmfit-py/

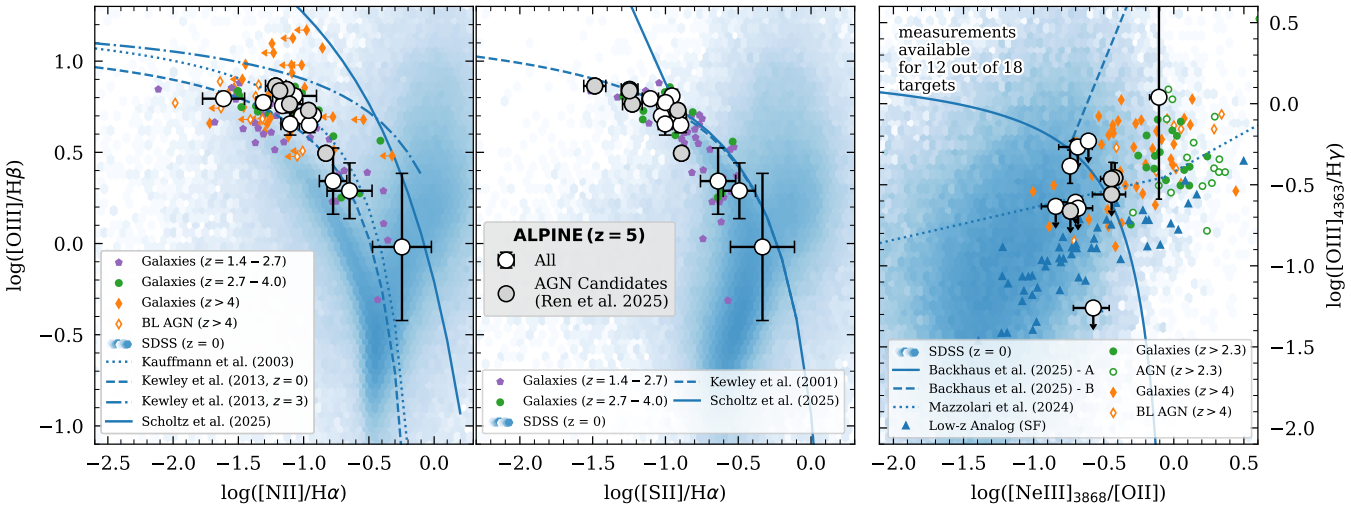

Figure 6. The 18 ALPINE-CRISTAL-JWST targets (large circles with type 1 AGN from W. Ren et al. 2025 indicated in gray) on different line ratio diagnostic diagrams. Left: $[\mathrm{N\,II}]_{6585}/\mathrm{H}\alpha$ BPT diagram. The AGN region is to the right of the dividing lines from G. Kauffmann et al. (2003; dotted), L. J. Kewley et al. (2013; dashed for $z = 0$ and dotted–dashed for $z = 3$, note that we do not show the parameterization for $z > 3$ as that would be an extrapolation to the study of L. J. Kewley et al. 2013), and J. Scholtz et al. (2025; solid; derived from A. Feltre et al. 2016; J. Gutkin et al. 2016). Observations from the literature at $z = 0$ (blue cloud, SDSS; K. N. Abazajian et al. 2009), at $z = 1.4$–2.7 (purple) and $z = 2.7$–4.0 (green) from the AURORA survey (A. E. Shapley et al. 2025), and at $z > 4$ (orange diamonds; Y. Harikane et al. 2023; K. Nakajima et al. 2023) are also shown. The target with the largest uncertainties and a $[\mathrm{N\,II}]_{6585}/\mathrm{H}\alpha$ close to unity is DC-873756, potentially a BPT-selected AGN (see the discussion in the text). Middle: $([\mathrm{S\,II}]_{6732} + [\mathrm{S\,II}]_{6718})/\mathrm{H}\alpha$ line ratio diagram. The AGN region is to the right of the dividing lines from L. J. Kewley et al. (2001; dashed) and J. Scholtz et al. (2025; solid; derived from K. Nakajima & R. Maiolino 2022). Observations from the literature at $z = 0$ (blue cloud, SDSS; K. N. Abazajian et al. 2009) and at $z = 1.4$–2.7 (purple) and $z = 2.7$–4.0 (green) from the AURORA survey (A. E. Shapley et al. 2025) are shown. Right: high-ionization auroral $[\mathrm{Ne\,III}]_{3868}/[\mathrm{O\,II}]$ vs. $[\mathrm{O\,III}]_{4363}/\mathrm{H}\gamma$ diagram. Only shown for 12 galaxies with robust $[\mathrm{Ne\,III}]_{3868}$ and $[\mathrm{O\,III}]_{4363}$ measurements. The AGN region is above the dividing line from G. Mazzolari et al. (2024; dotted) or to the right of the combined dividing lines by B. E. Backhaus et al. (2025; dashed and solid). The region in the upper left above the dashed and solid lines may contain star-forming galaxies and AGN (see B. E. Backhaus et al. 2025). The target with the largest uncertainty and $[\mathrm{Ne\,III}]_{3868}/[\mathrm{O\,II}]$ close to unity is DC-742174, a metal-poor compact multicomponent system.

and high redshifts (Y. Harikane et al. 2023; K. Nakajima et al. 2023; A. E. Shapley et al. 2025). We find that none of the targets are robustly identified as AGN based on these line diagnostic diagrams. However, they do reside close to the AGN versus star-forming galaxy dividing lines, in agreement with other measurements from the literature (see the figure caption) and expectations from lower redshift analogs (see A. L. Faisst et al. 2018). We note that the separation lines by L. J. Kewley et al. (2013) and J. Scholtz et al. (2025) in the classic BPT diagram (left panel in Figure 6) take into account the stronger ionization in high-redshift galaxies compared to galaxies at lower redshifts (e.g., L. J. Kewley et al. 2001). In other words, the separation of star-forming galaxies and AGN includes the harder radiation in star-forming early galaxies. The fact that the ALPINE-CRISTAL galaxies are well below these dividing lines suggests that they might be evolved enough to resemble more lower redshift galaxies. Two galaxies are worth mentioning in more detail.

DC-873756 is the only galaxy that lies in the AGN region (based on the G. Kauffmann et al. 2003 and L. J. Kewley et al. 2013 parameterizations) of the classical $[\mathrm{N\,II}]_{6585}/\mathrm{H}\alpha$ versus $[\mathrm{O\,III}]_{5007}/\mathrm{H}\beta$ BPT diagram (however, it is not an outlier in the other diagrams or in the J. Scholtz et al. 2025 parameterization). It is not identified as a type 1 AGN. DC-873756 is a peculiar galaxy, showing a compact core with a strong dust continuum emission offset from the diffuse stellar continuum. Its spectrum shows a $[\mathrm{N\,II}]_{6585}/\mathrm{H}\alpha$ ratio close to unity, but due to the dust obscuration, the bluer emission lines are weak, which affects its reliability on the other two diagnostic diagrams (see Figure B1). Taken at face value, this galaxy could be an AGN candidate, but deeper observations are needed for confirmation.

DC-742174 is a relatively compact system with at least three components. It is an outlier on the $[\mathrm{Ne\,III}]_{3868}/[\mathrm{O\,II}]$ versus $[\mathrm{O\,III}]_{4363}/\mathrm{H}\gamma$ diagram, showing a logarithmic $[\mathrm{Ne\,III}]_{3868}/[\mathrm{O\,II}]$ line ratio close to unity. This system is not an outlier on the other diagrams and also not a type 1 AGN candidate based on the work by W. Ren et al. (2025). The increased $[\mathrm{Ne\,III}]_{3868}$ could therefore originate from a low metallicity due to the monotonic anticorrelation of $[\mathrm{Ne\,III}]_{3868}$ with oxygen abundance (T. Nagao et al. 2006; E. Pérez-Montero et al. 2007; F. Shi et al. 2007). In fact, the $[\mathrm{Ne\,III}]_{3868}/[\mathrm{O\,II}]$ ratio of DC-742174 is in the upper range of the distribution of MOSDEF galaxies (A. E. Shapley et al. 2017; M.-S. Jeong et al. 2020) if compared to a similar mass of $\log(M_*/M_\odot) = 9.6$. Its low metallicity is indeed also suggested by the strong-line method (see below), finding a $12 + \log(\mathrm{O/H}) \sim 7.84$, and also consistent with a weak $[\mathrm{C\,II}]$ emission (Figure B1). Another possibility (likely related to low metallicity) could be a harder radiation field, which is also found in high equivalent-width emission-line galaxies (e.g., A. A. Khostovan et al. 2024).

4.4. Velocity Maps

With the present NIRSpec/IFU observations we are in a unique position to study for the first time the kinematics of the ionized gas in these post-EoR galaxies. To showcase the potential of the ALPINE-CRISTAL-JWST survey in this regard, we show in Figure 7 the ionized gas velocity maps, which are based on the $\mathrm{H}\alpha$ fluxes for each of the targets. We first apply the emission-line-based mask (see Section 4.2) to the cube and then fit the $\mathrm{H}\alpha$ centroid in each spatial pixel using the same methods as described in Section 4.3. Note that the optical velocity resolution (50–70 $\mathrm{km\,s^{-1}}$) is worse than

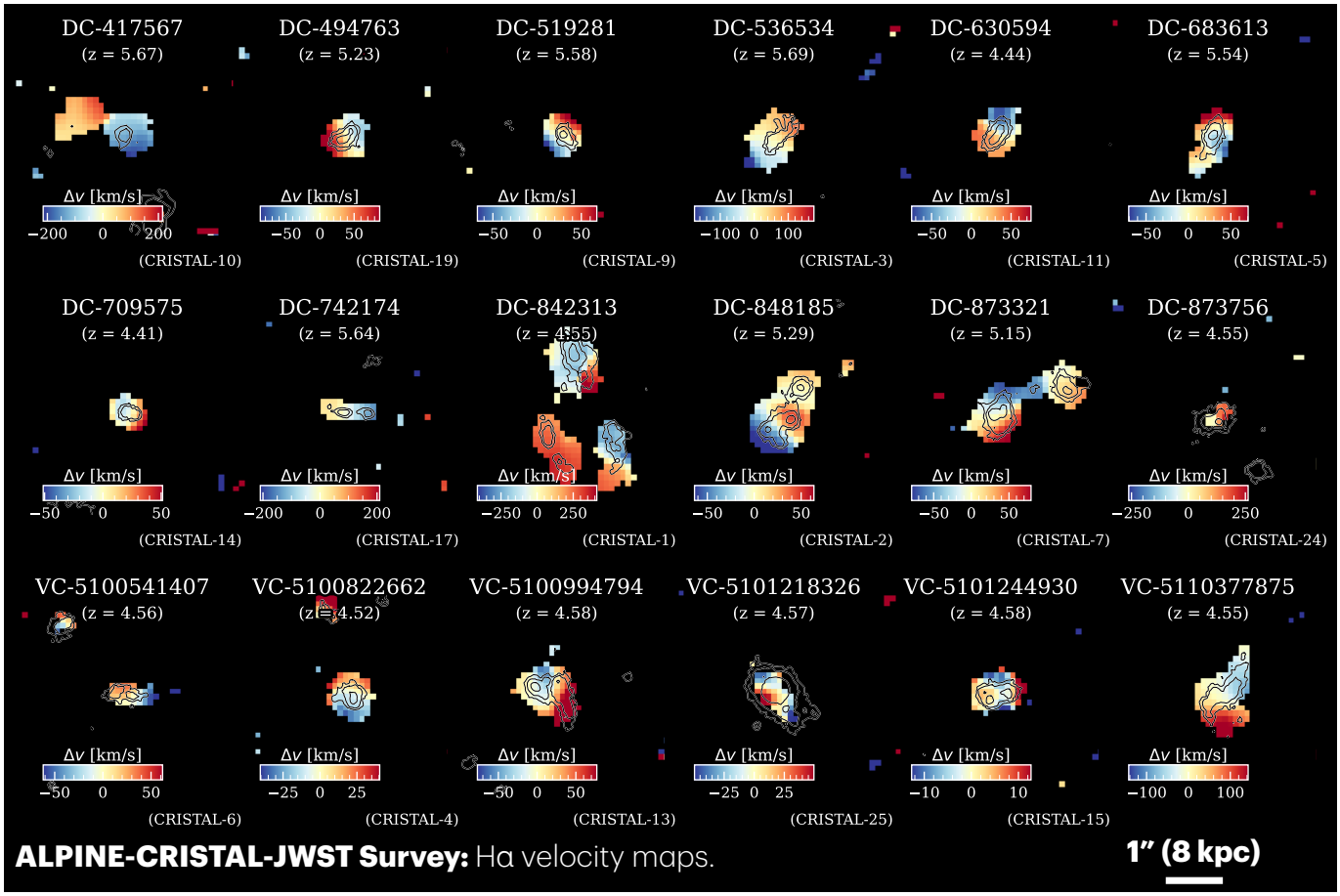

Figure 7. Collage of the Hα velocity maps of the 18 targets in the ALPINE-CRISTAL-JWST sample. The stellar continuum from the COSMOS-Web JWST/NIRCam F277W imaging is shown with contours (5σ, 10σ, and 30σ).

obtained with [C II] with ALMA (10–20 km s^{-1}; G. C. Jones et al. 2021; M. Romano et al. 2021; R. Herrera-Camus et al. 2022; K. Telikova et al. 2025; A. Posses et al. 2025). A collage of these Hα-based velocity maps for each of the 18 targets is shown in Figure 7 (in units of kilometers per second). Detailed [C II]-based velocity maps will be presented in L. L. Lee et al. (2025). Simulations suggest that the inferred V/σ (rotation versus dispersion) ratio may vary significantly depending on which line tracer (i.e., ionized or neutral gas) is used (e.g., M. Kohandel et al. 2020, 2024). Observational results are still limited due to the lack of simultaneous observations of ionized and neutral gas tracers. Using a single line tracer could bias the interpretation of galaxy dynamics, making multiwavelength data needed for a comprehensive physical picture of galaxy dynamics. On the other hand, investigating the velocity structure of cold and hot gas disks may tell us about disk formation. To first order, we find a similar velocity structure between Hα and [C II], showing some ordered rotation as well as mergers (e.g., A. L. Danhaive et al. 2025; L. L. Lee et al. 2025; E. Wisnioski et al. 2025). The fraction of disk-dominated systems is around 40%–50% as measured by [C II] (G. C. Jones et al. 2021; M. Romano et al. 2021; K. Telikova et al. 2025) and Hα (K. Telikova et al. 2025; L. L. Lee et al. 2025) for the ALPINE/CRISTAL sample. A more detailed comparison between the ionized gas (Hα) and the cold ISM gas (as traced by [C II]) will be presented in a forthcoming paper.

4.5. Nebular Dust Attenuation

The nebular dust attenuation differs from the stellar attenuation due to the configuration of clouds in the ISM (e.g., D. Calzetti 2001; N. A. Reddy et al. 2015; S. Salim & D. Narayanan 2020; N. A. Reddy et al. 2025). The differential dust attenuation[76] between nebular and stellar light is therefore an important quantity for many science applications (see the discussion by A. L. Faisst et al. 2019). With JWST spectroscopic observations, we can now derive the nebular dust attenuation of our targets through the Hα/Hβ Balmer decrement via

$$E_n(B-V) = \frac{2.5}{(k_\lambda(\mathrm{H}\beta) - k_\lambda(\mathrm{H}\alpha))} \log(R/R_0), \quad (1)$$

where k_λ(Hα) and k_λ(Hβ) are the reddening curve values at the wavelength of Hα and Hβ, respectively. R and R_0 are the observed and intrinsic $\frac{\mathrm{H}\alpha}{\mathrm{H}\beta}$ flux ratio, respectively. From that, any observed emission-line flux (F_o^{line}) can be translated into an intrinsic line flux (F_i^{line}) by correcting for the presence of galaxy-intrinsic dust via

$$F_i^{\mathrm{line}}(\lambda) = F_o^{\mathrm{line}}(\lambda) \times 10^{0.4\, E_{\mathrm{n}}(B-V)\, k(\lambda)}. \quad (2)$$

[76] The differential dust attenuation between stars and nebular lines is defined as $f_{\mathrm{dust}} = E_{\mathrm{s}}(B-V) \,/\, E_{\mathrm{n}}(B-V)$.

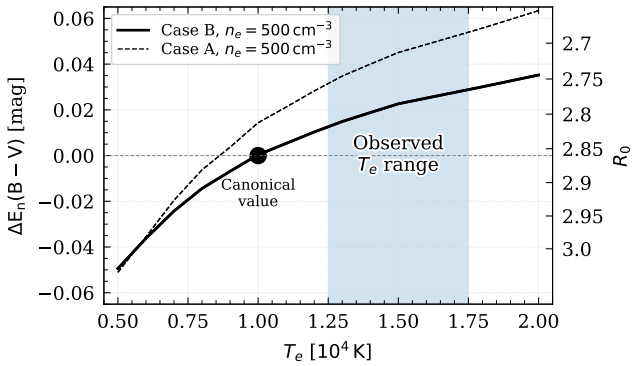

Figure 8. Dependence of nebular dust attenuation (left y-axis) derived from the $\frac{\mathrm{H}\alpha}{\mathrm{H}\beta}$ Balmer decrement on electron temperature (T_e) and recombination type (case A: dashed line; case B: solid line) using `PyNeb`. The right y-axis shows the R_0 value with the canonical value of 2.86 (for case B and $T_e = 10^4$ K highlighted). Note that the dependence on electron density (n_e) is insignificant. The blue area shows the observed T_e range measured for ALPINE-CRISTAL-JWST galaxies with auroral line detections (see A. Faisst et al. 2025).

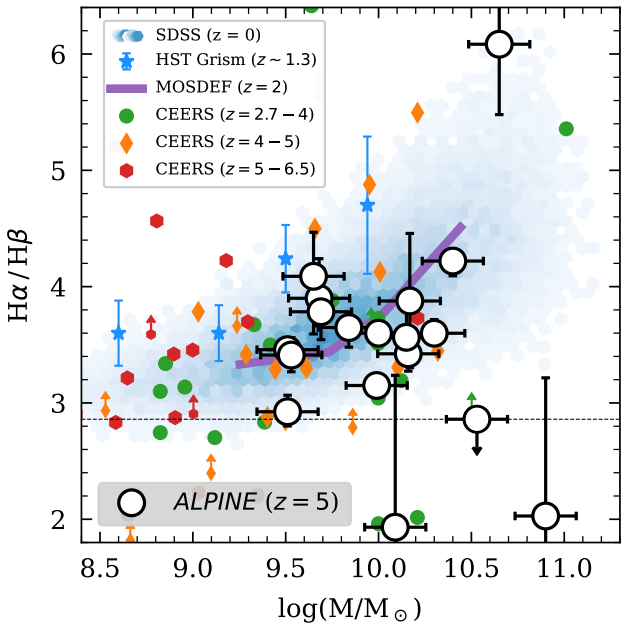

Figure 9. Relation between $\mathrm{H}\alpha/\mathrm{H}\beta$ total line flux ratios and stellar mass. The ALPINE-CRISTAL-JWST $z \sim 5$ observations are shown as large symbols together with data at $z \sim 0$ (SDSS, total stellar masses, blue background; K. N. Abazajian et al. 2009), at $z \sim 1.3$ (HST grism, blue stars; A. J. Battisti et al. 2022), at $z \sim 2$ (MOSDEF, purple line; A. E. Shapley et al. 2022), and at $z > 2.7$ (CEERS, other symbols, see A. E. Shapley et al. 2023). The expected $\mathrm{H}\alpha/\mathrm{H}\beta$ line ratio for case B recombination is shown as a dashed horizontal line.

We assumed a reddening curve $k(\lambda)$ similar to local starburst galaxies (D. Calzetti et al. 2000), motivated by the fact that the ALPINE galaxies are relatively metal enriched (see Section 4.6), even though some evolution of the dust properties are suggested by works measuring the dust attenuation curve (R. Fisher et al. 2025; V. Markov et al. 2025). Note that the intrinsic flux ratio R_0 varies on the assumption of electron temperature, density, and recombination type (case A and B). Specifically, case B is valid for a medium that is optically thick where recombination to the ground state is ignored as the ionizing photons are absorbed locally ("on-the-spot" approximation). Vice versa, case A is expected in an optically thin cloud (see discussion in O. Nebrin 2023).

Usually, a canonical value of $R_0 = 2.86$ is assumed (J. A. Cardelli et al. 1989), which is valid for case B recombination and $T_e = 10^4$ K. In Figure 8, we show how R_0, and the corresponding difference in $E_n(B-V)$, change with respect to these canonical values as a function of T_e for both case A and B recombination. The curves are derived using the `PyNeb` Python package (V. Luridiana et al. 2015) with the P. J. Storey & D. G. Hummer (1995) atomic database and for $n_e = 500\,\mathrm{cm}^{-3}$ (consistent with observations of the ALPINE galaxies; B. N. Vanderhoof et al. 2022; A. Faisst et al. 2025; E. Veraldi et al. 2025). In the following, we quote the $E_n(B-V)$ values (and use this as dust correction) for the canonical emission-line dust correction (case B, $T_e = 10^4$ K) for simplicity and for comparison to other works. However, we caution that the quoted $E_n(B-V)$ values could be underestimated by up to 0.04–0.05 mag (although smaller than measurement errors) due to *lower* R_0 values assuming the observed T_e range (blue area in Figure 8, see also A. Faisst et al. 2025 and I. DeLooze et al. 2025, in preparation, where T_e is derived from fainter auroral lines). Lower values can also be achieved through Balmer self-absorption such as suggested in low-mass strong-line emitters (H. Atek et al. 2009; H. Yang et al. 2017; N. Pirzkal et al. 2023; C. Scarlata et al. 2024). The final values of $E_n(B-V)$ of the galaxies in our sample are listed in Table A2.

We also compared the $E_n(B-V)$ values to the stellar dust attenuation values, $E_s(B-V)$, derived from SED fitting (A. Tsujita et al. 2025). We find a differential dust attenuation (f_{dust}), which is consistent with the value measured for local starburst galaxies ($f_{\mathrm{dust}} = 0.44$; D. Calzetti et al. 2000). However, we note that this is a spatial integrated average and locally the differential dust attenuation may vary. This is discussed in detail by A. Tsujita et al. (2025).

Figure 9 suggests that the relation between the $\mathrm{H}\alpha/\mathrm{H}\beta$ line ratio and stellar mass is not evolving significantly with cosmic time since $z = 5$. We find a similar relation to that found by the MOSDEF survey ($z \sim 2$; N. A. Reddy et al. 2015; A. E. Shapley et al. 2022) and the $z \sim 0$ galaxy population from SDSS (using the total masses; K. N. Abazajian et al. 2009). However, we find generally lower values compared to the study by A. J. Battisti et al. (2022), focusing on $z = 1.3$ galaxies observed with HST grism. Note that using SDSS fiber stellar masses (instead of total masses) would move the $z = 0$ cloud to ~0.4 dex lower stellar masses, making it consistent with the $z = 1.3$ measurements from A. J. Battisti et al. (2022). Literature studies at similar redshifts of $z = 4$–6 (A. E. Shapley et al. 2023) are consistent with our measurements when extrapolating the relation from their lower stellar masses to the higher stellar masses probed by the ALPINE-CRISTAL-JWST survey sample. For two galaxies (VC-5100541407 and VC-5101218326) we find $\mathrm{H}\alpha/\mathrm{H}\beta$ line ratios that are below the canonical case B value of 2.86. This could mean either hotter temperatures (Figure 8) or that case B is not valid in these cases (see the discussion in C. Scarlata et al. 2024). However, we caution to draw such conclusions as the measurement uncertainties are significant and the values are consistent at the 1σ-level with the case B value. We note that there are also several CEERS galaxies that show $\mathrm{H}\alpha/\mathrm{H}\beta$ values smaller than the canonical value. A. E. Shapley et al. (2023) argue that the majority of these cases are due to the remaining systematics in the NIRSpec grating-to-grating flux calibration. The upper

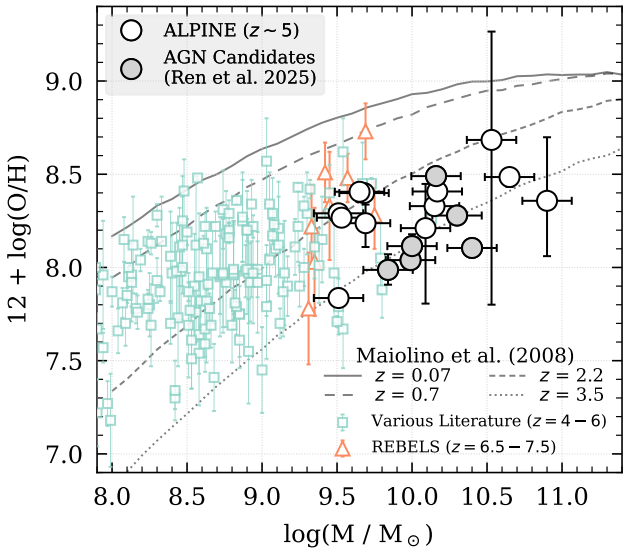

Figure 10. The stellar mass vs. metallicity relation of the $z \sim 5$ ALPINE-CRISTAL-JWST sample. Other observations with JWST at $z = 4$–6 (aqua open squares; see the text for references) and at $z = 6.5$–7.5 (gold triangles; from the REBELS-IFU sample, L. E. Rowland et al. 2025) are also shown. The lines show the parameterizations by R. Maiolino et al. (2008) at $z \lesssim 3.5$. The gray large symbols show ALPIEN-CRISTAL-JWST type 1 AGN candidates by W. Ren et al. (2025).

limit (hatched circle) is DC-873756, a potential BPT-selected AGN with uncertain Hα measurement and weak Hβ flux due to significant dust attenuation in the central core as suggested by the ALMA dust continuum detection.

4.6. Strong-line Metallicity Measurement

We measured the gas-phase metallicity, defined as $Z_{\rm neb} \equiv 12 + \log({\rm O/H})$, of our galaxies using the strong optical emission lines detected for all individual galaxies. In A. Faisst et al. (2025), we investigated T_e-based metallicities and the comparison of different strong-line calibrations in more detail.

Here, we measured the spatially integrated metal content of the galaxies using strong optical lines such as [O II], Hβ, and [O III] using the calibration revisited by R. L. Sanders et al. (2024). Specifically, we derived a best-fit metallicity for each galaxy by jointly fitting the line ratios $R_{23} \equiv$ ([O III]$_{5007}$ + [O III]$_{4959}$ + [O II]$_{3727}$)/Hβ, $R_2 \equiv$ [O II]$_{3727}$/Hβ, $O_{32} \equiv$ [O III]$_{5007}$/[O II]$_{3727}$, and $R_3 \equiv$ ([O III]$_{5007}$ + [O III]$_{4959}$)/Hβ to the R. L. Sanders et al. (2024) parameterizations. All emission-line ratios were corrected for dust attenuation assuming the D. Calzetti et al. (2000) reddening curve and $E_n(B-V)$ as derived in Section 4.5. The measured emission-line ratios for each galaxy are listed in Table A3. We first used the parameterization from R. L. Sanders et al. (2024) and derive a $\chi^2(Z_{\rm neb})$ value for a grid of metallicities for each of the line ratios. To obtain the final best-fit metallicity and uncertainties, we combined the χ^2 results and computed the 16–50–84 percentiles. The final strong-line metallicity measurements are listed in Table A2. We note that using all the above line ratios could lead to overfitting (as they are not independent of each other). We tested the impact of this on our final results by refitting the line ratios only using the combinations $R_2 + O_{32}$ or $R_3 + O_{32}$. We found that the metallicity measurements differ by less than 0.05 dex in $12 + \log({\rm O/H})$, an overall difference of $<1\sigma$.

Figure 10 shows the stellar mass versus metallicity relation for our ALPINE-CRISTAL-JWST survey targets. The measured abundances range from 7.7 to 8.5 in $12 + \log({\rm O/H})$, corresponding to 10%–70% of solar metallicity.[77] We compared our measurements at $z \sim 5$ to observations at other redshifts. These include the mass–metallicity parameterization from R. Maiolino et al. (2008; based on T. Nagao et al. 2006) at $z < 3.5$, measurements from the REBELS-IFU sample at $z = 6.5$–7.5 (L. E. Rowland et al. 2025), and various other observations with JWST from the literature at $z = 4$–6 (including M. Curti et al. 2023; K. Nakajima et al. 2023; A. Marszewski et al. 2024; T. Morishita et al. 2024; A. Sarkar et al. 2025). Note that the metallicity measurements at $z > 6.5$ are mainly based on [O III] and [O II], while the ones derived for our sample are based on a combination of all strong optical lines. Overall, we find that the ALPINE-CRISTAL-JWST galaxies, which lie at the higher mass end of the galaxy distribution at these redshifts, are $\sim$0.5 dex more metal enriched than galaxies at the same redshifts at lower stellar masses of $\log(M_*/M_\odot) < 9$. However, we do not find a significant evolution in metal abundances between $z = 3.5$ and 7.5 at a given stellar mass, emphasizing that early galaxies must already be significantly metal enriched. The detailed comparison of these findings to analytical and cosmological models are presented in A. Faisst et al. (2025). In addition, spatially resolved metallicity measurements are presented in S. Fujimoto et al. (2025) as well as in other future works.

4.7. Comparison of Different Star Formation Indicators

Figure 11 shows a comparison between the different SFR indicators discussed in Section 3.5. To first order, we find a good agreement between Hα-derived SFRs and SFRs based on SED fitting and UV+FIR luminosity (left panel), [O II] emission (middle panel), and [C II] (right panel; using the calibration by D. Schaerer et al. 2020). To second order, we find an increased scatter with an amplitude of a factor of 5 or more between [C II] or continuum-based/SED-based SFR and Hα or [O II]-based SFRs. The scatter is toward *higher* Hα or [O II] SFRs. This systematic scatter can be explained naturally by a bursty star formation, which is common in star-forming galaxies at high redshifts (e.g., A. L. Faisst et al. 2019; V. Mehta et al. 2023; R. Endsley et al. 2025; R. Navarro-Carrera et al. 2024; G. Sun et al. 2025). For example, A. L. Faisst et al. (2019) measured similar discrepancies between Hα- and SED-based SFR measurements for a large sample of $z = 4.5$ galaxies. (Although note that in this case Hα was measured from Spitzer [3.6 μm]–[4.5 μm] colors with an unknown $f_{\rm dust}$, which caused significant uncertainties.) Hα is tied to ionized gas around star-forming regions and correlates directly with star formation on timescales of $\sim$10 Myr (e.g., R. C. Kennicutt 1998). [C II] is expected to be emitted in various ISM phases, hence a correlation with star formation similar to the UV or far-IR continuum is expected (I. De Looze et al. 2011; R. Herrera-Camus et al. 2015). For the dependence of the Hα versus [C II] SFR relation with burstiness, see also the theoretical work by E. Veraldi et al. (2025). We find three outliers (DC-873756, VC-5100541407, and VC-5101218326) with significantly larger uncertainties in Hα. The first one is

[77] We assume here a solar value of $12 + \log({\rm O/H}) = 8.69$ (C. Allende Prieto et al. 2001); however, note that this value could be higher (M. Bergemann et al. 2021).

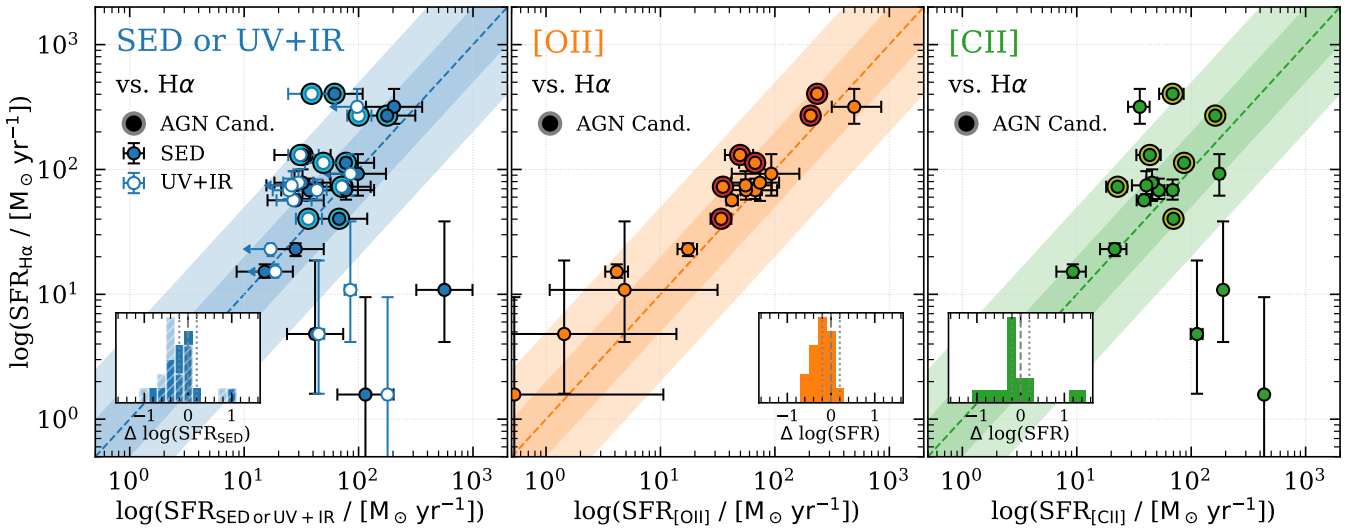

Figure 11. Comparison of different star formation indicators to Hα (SED- and UV+IR-based, left; [O II]-based, middle; [C II]-based, right). Limiting UV+IR-based SFRs are given for upper limits in L_{IR} (left panel, empty symbols). The dark (light) bands show a factor of 2 (5) deviation from the one-to-one relation. The scatter between SED- and [C II]-based SFR compared to Hα SFRs may be due to the different SFR timescales probed by these indicators. The inset shows histograms of the logarithmic difference in SFRs (negative values meaning higher Hα SFR). The dashed line indicates the median, while the dotted lines show the 1σ range. Type 1 AGN candidates from W. Ren et al. (2025) are indicated by larger symbols (see also Section 2.2). Note that these are consistent with the expected relations.

the potential BPT-detected AGN (Figure 6). The other two seem to be significantly dust obscured according to their ALMA far-IR continuum. Consequently, they show a lower SNR in [O II], Hβ, and [O III] line emission, which increases the uncertainty in the nebular dust correction measurement, which in turn leads to an underestimation of their dust-corrected Hα- and [O II]-based SFRs.

4.8. Extended Hα Emission at z = 5

In addition to the study of spatially integrated properties outlined in this paper, JWST's IFU observations open the door for new cutting-edge studies of the enrichment of the CGM around high-redshift galaxies. So far, extended halos of carbon-enriched warm gas have been traced by [C II] emission out to as far as 10 kpc (e.g., S. Fujimoto et al. 2019). Only now with NIRSpec/IFU data, we are able to trace the ionized gas structure out to similar radii. This allows unique comparisons of the extended UV (ionized by young stars), Hα (ionized gas), and [C II] (warm gas) and their comparison to simulations to inform feedback prescriptions and the abundance of satellite galaxies to ultimately study the origin of these halos (e.g., M. Ginolfi et al. 2020; E. Pizzati et al. 2020, 2023; N. Muñoz-Elgueta et al. 2024; M. Romano et al. 2024; A. Schimek et al. 2024; J. E. Birkin et al. 2025; R. Ikeda et al. 2025).

Figure 12 shows the stacked UV, Hα, and [C II] radial profiles obtained from a subsample of isolated, nonmerging galaxies from the ALPINE-CRISTAL-JWST sample (DC-494763, DC-519281, DC-630594, DC-709575, VC-5100822662, and VC-5101218326). A two-component fit (inset) confirms Hα disk components with twice as large effective radii compared to continuum emission. This suggests the extent of the ionized medium into the CGM, either due to surrounding star-forming regions (e.g., star-forming satellites) or ionization of gas from the young stellar population in the central galaxy. We can also see that the [C II] emission is more extended than the Hα emission (and significantly more than the UV emission) suggesting maintained [C II] halos far out into the CGM. This is consistent with a relatively enriched CGM at similar levels of the ISM

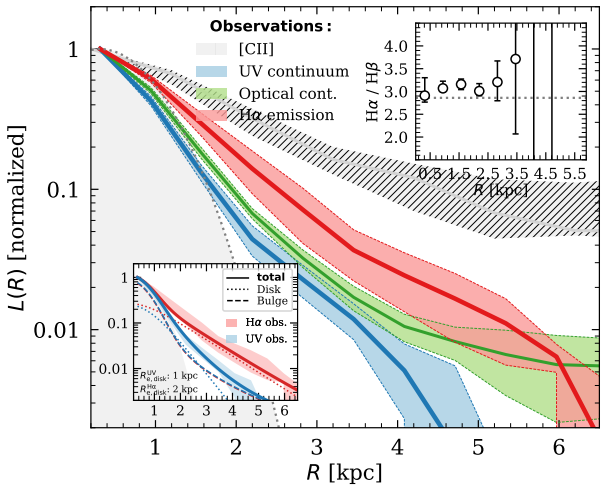

Figure 12. Average [C II] (gray, hatched), UV continuum (blue), optical continuum (green), and Hα (red) radial profiles (thick lines with 1σ uncertainty). The profiles are normalized to their peak intensity. Only isolated and compact galaxies have been used (see the text). The gray region shows the IFU spatial PSF profile. The upper right inset shows the average radial profile of the Hα/Hβ flux ratio, suggesting a relatively constant radial dust attenuation. The lower left inset shows the decomposition of the UV (light blue) and Hα (light red) radial profiles in a disk ($n_{Sersic} = 1$, dotted) and bulge ($n_{Sersic} = 4$, dashed) component. The bulge components have the same half-light radius, while $R^{H\alpha}_{e,disk} \sim 2 \times R^{UV}_{e,disk}$.

(W. Wang et al. 2025, in preparation) and a comparison with simulations suggests that outflows may play a role more significant than satellite galaxies in this enrichment process (L.-J. Liu et al. 2025, in preparation).

5. Summary and Future Work

In this paper, we have introduced the ALPINE-CRISTAL-JWST survey, a benchmark survey to study the spatially resolved properties of the ISM and CGM of typical main-sequence $z = 4$–6 galaxies at $\log(M_*/M_\odot) > 9.5$. The unique combination of HST, JWST, and ALMA enables for the first time the observations of stars, dust, and gas at UV through

far-IR wavelengths at comparable spatial resolution of ∼1 kpc. Only with such a multiwavelength exploration we can progress our understanding of the intertwined physical processes in galaxies at early times. Located right at the post-EoR cosmic time, the ALPINE-CRISTAL-JWST survey provides the necessary link between primordial galaxy evolution during the EoR ($z > 6$) and mature galaxy evolution at cosmic noon ($z = 2$–3). Furthermore, it complements studies of JWST-detected galaxies at lower stellar masses. For example, we show that the metal content of galaxies across all masses evolves little between $z = 5$ and cosmic noon. This is discussed in more detail in A. Faisst et al. (2025).

The ALPINE-CRISTAL-JWST survey helps answer many open questions regarding the ISM and CGM properties of post-EoR galaxies, including how and where stars are formed, how their ISM is built up, and how the CGM is enriched. The survey also sheds light on the contribution of faint AGN to the typical galaxy population at these redshifts.

In addition to the spatial integrated properties outlined in this paper, JWST's IFU enables new resolved observations of the rest-frame optical light, which, combined with imaging and ALMA observations on similar spatial scales, will lead surely to new scientific discoveries. This includes the measurement of the star formation burstiness in different parts of the galaxies through the spatially resolved Hα/UV continuum emission ratio (A. Hadi et al. 2025, in preparation), reflecting bursts of star formations (e.g., A. L. Faisst et al. 2019). Another interesting avenue of research may be extended Hα halos and their connection to UV and [C II] emission (see Section 4.8). The study of the multiphase gas (ionized, warm, and neutral) in the halos of these galaxies provide unique insights into the processes of feedback (stellar and AGN), outflow, and the existence of satellite galaxies in enriching the CGM of these galaxies. The comparison to state-of-the-art simulations (L.-J. Liu et al. 2025, in preparation) will enable us to gain a comprehensive picture of these processes and their impact on early galaxy formation and evolution.

In addition to these interesting avenues, the ALPINE-CRISTAL-JWST survey will enable future science investigations capitalizing on its unique combination of the spectral and spatial resolution and multiwavelength coverage of different cutting-edge facilities:

I. The integrated stellar mass versus metallicity relation and its comparison to state-of-the-art model predictions is further discussed in A. Faisst et al. (2025).
II. Resolved metallicity abundances and gradients as well as the spatially resolved relation between metallicity, SFR, and stellar mass density is discussed in the ALPINE-CRISTAL-JWST data reduction paper by S. Fujimoto et al. (2025) as well as in L. L. Lee et al. (2025).
III. The discovery of low-luminosity type 1 (broad line) AGN and their black hole masses are presented in W. Ren et al. (2025).
IV. A comprehensive investigation of the difference in the chemical properties of the ISM and CGM will be presented in W. Wang et al. (2025, in preparation).
V. The study of the resolved stellar and nebular dust attenuation is presented in A. Tsujita et al. (2025).
VI. The properties of star formation driven outflows and their role in producing the first massive quiescent galaxies will be discussed in R. Davies et al. (2025, in preparation).
VII. The metallicity dependence of the [C II] versus FIR luminosity ratio will be studied to understand [C II] deficits (R. Herrera-Camus et al. 2025, in preparation).
VIII. A spatial study of star formation burstiness and comparison to theoretical models will be carried out in A. Hadi et al. (2025, in preparation).
IX. A detailed investigation of the (spatially resolved) relation between [C II] and SFR is, and will be, carried out in C. Accard et al. (2025), M. Palla et al. (2025, in preparation), and Y. Li et al. (2025, in preparation).
X. Spatially resolved scaling relations including dust masses and dust temperatures will be studied in F. Lopez et al. (2025, in preparation) and M. Relano et al. (2025, in preparation).
XI. The relation between N/O and O/H will be studied in I. DeLooze et al. (2025, in preparation).

Additional studies will focus on the spectroscopic properties of star-forming clumps, constraining the IMF, the comparison of the kinematics of low and high-ionization gas as traced by [C II] and optical lines, the detailed spatially resolve star formation history modeling including spectroscopic data (see also J. Li et al. 2024), the study of dust production mechanisms, and the characterization of spatial changes in the ionization parameter ($\xi_{\rm ion}$) that can inform the reionization of neutral hydrogen by galaxies in the EoR.

Acknowledgments

This work is based in part on observations made with the NASA/ESA/CSA James Webb Space Telescope. The JWST and HST data presented in this article were obtained from the Mikulski Archive for Space Telescopes (MAST) at the Space Telescope Science Institute. These observations are associated with programs, HST-GO-13641 (doi:10.17909/xne1-7v26), JWST-GO-01727 (doi:10.17909/ph8h-qf05), JWST-GO-03045 (doi:10.17909/cqds-qc81), and JWST-GO-04265 (doi:10.17909/wac6-9741). This research has made use of the NASA/IPAC Infrared Science Archive (IRSA), which is funded by the National Aeronautics and Space Administration and operated by the California Institute of Technology. The following data set was used from IRSA: COSMOS Project (2020). Support for program JWST-GO-03045 was provided by NASA through a grant from the Space Telescope Science Institute, which is operated by the Association of Universities for Research in Astronomy, Inc., under NASA contract NAS 5-03127. This work made use of Astropy,[78] a community-developed core Python package and an ecosystem of tools and resources for astronomy (Astropy Collaboration et al. 2013, 2018; Astropy Collaboration et al. 2022). This paper makes use of the following ALMA data: ADS/JAO.ALMA#2017.1.00428.L, #2019.1.00226.S, #2022.1.01118.S, and #2021.1.00280.L. ALMA is a partnership of ESO (representing its member states), NSF (USA) and NINS (Japan), together with NRC (Canada), MOST and ASIAA (Taiwan), and KASI (Republic of Korea), in cooperation with the Republic of Chile. The Joint ALMA Observatory is operated by ESO, AUI/NRAO, and NAOJ. M.A. is supported by FONDECYT grant No. 1252054 and gratefully acknowledges support from ANID Basal Project FB210003 and ANID MILENIO NCN2024_112. M.B. gratefully acknowledges support from the ANID BASAL project

[78] http://www.astropy.org

FB210003 and from the FONDECYT regular grant 1211000. S.F. acknowledges support from NASA through the NASA Hubble Fellowship grant HST-HF2-51505.001-A awarded by the Space Telescope Science Institute, which is operated by the Association of Universities for Research in Astronomy, Incorporated, under NASA contract NAS5-26555. R.J.A was supported by FONDECYT grant No. 1231718 and by the ANID BASAL project FB210003. D.R. gratefully acknowledges support from the Collaborative Research Center 1601 (SFB 1601 subprojects C1, C2, C3, and C6) funded by the Deutsche Forschungsgemeinschaft (DFG)—500700252. R.A. acknowledges financial support from projects PID2023-147386NB-I00 and the Severo Ochoa grant CEX2021-001131-S funded by MCIN/AEI/10.13039/501100011033 K.T. acknowledges support from JSPS KAKENHI grant No. 23K03466. V.V. acknowledges support from the ANID BASAL project FB210003 and from ANID—MILENIO—NCN2024_112. M.S. was financially supported by Becas-ANID scholarship #21221511 and also acknowledges support from ANID BASAL project FB210003. M.P acknowledges financial support from the project "LEGO—Reconstructing the building blocks of the Galaxy by chemical tagging" granted by the Italian MUR through contract PRIN2022LLP8TK_001. J.M. gratefully acknowledges support from ANID MILENIO NCN2024_112. G.C.J. acknowledges support by the Science and Technology Facilities Council (STFC), by the ERC through Advanced grant 695671 "QUENCH," and by the UKRI Frontier Research grant RISEandFALL. R.L.D. is supported by the Australian Research Council through the Discovery Early Career Researcher Award (DECRA) Fellowship DE240100136 funded by the Australian Government. E.d.C. acknowledges support from the Australian Research Council through project DP240100589. E.I. gratefully acknowledges financial support from ANID - MILENIO - NCN2024_112 and ANID FONDECYT Regular 1221846. A. F. is partly supported by the ERC Advanced grant INTERSTELLAR H2020/740120, and by grant NSF PHY-2309135 to the Kavli Institute for Theoretical Physics. M.R. acknowledges support from project PID2023-150178NB-I00 financed by MCIU/AEI/10.13039/501100011033, and by FEDER, UE. L.V. acknowledges support from the INAF Minigrant "RISE: Resolving the ISM and Star formation in the Epoch of Reionization" (PI: Vallini, Ob. Fu. 1.05.24.07.01). This work was supported by the French government through the France 2030 investment plan managed by the National Research Agency (ANR), as part of the Initiative of Excellence of Université Cote d'Azur under reference number ANR-15-IDEX-01. We acknowledge the Lorentz Center for giving us the opportunity and infrastructure to organize a successful and very stimulating workshop, which discussions helped to realize this work.

Facilities: IRSA, HST (ACS, WFC3/IR), JWST (NIRCam, NIRSpec), ALMA.

Software: `Astropy` (Astropy Collaboration et al. 2013, 2018; Astropy Collaboration et al. 2022), `PyNeb` (V. Luridiana et al. 2015), `CIGALE` (D. Burgarella et al. 2005; M. Boquien et al. 2019), `Bagpipes` (A. C. Carnall et al. 2018; A. C. Carnall et al. 2019), `MAGPHYS` (E. da Cunha et al. 2008; E. da Cunha et al. 2015).

Appendix A
Tables

The following tables describe a summary of the targets and available data (Table A1), a summary of physical measurements (Table A2), and a list of measured emission-line ratios (Table A3) and line fluxes (Table A4).

Table A1
Summary of Targets and Available Data

Name		JWST		HST	ALMA
ALPINE	CRISTAL	Spec.	Imaging	Spec./Imag.	
DC-417567	CRISTAL-10	**3045**, 5974, 6480	⋯	9822, 16443, 13641	2012.1.00523.S, 2017.1.00428.L, 2021.1.00280.L, 2019.1.00459.S
DC-494763	CRISTAL-20	**3045**, 5893	1727	9822, 13657, 16259, 16443, 16684, 17802	2017.1.00428.L, 2021.1.00280.L, 2023.1.00180.L
DC-519281	CRISTAL-09	**3045**, 5974, 5893	1727	9822, 12578, 13669, 14114, 16443, 17802	2017.1.00428.L, 2021.1.00280.L
DC-536534	CRISTAL-03	**3045**, 5893	1727	9822, 12578, 13641, 16259, 16443 16684, 17802	2012.1.00523.S, 2017.1.00428.L, 2021.1.00280.L, 2023.1.00180.L
DC-630594	CRISTAL-11	**3045**, 5893, 6368	1727, 1837, 1840, 2321, 2514	9822, 12440, 12328, 15100, 15647, 17802	2013.1.01292.S, 2015.1.00379.S, 2017.1.00428.L, 2021.1.00280.L, 2021.1.00225.S
DC-683613	CRISTAL-05	**3045**, 5893, 5974	1727, 1837, 5893	9822/9999, 12328, 13641, 13657, 15100, 16443, 17802	2012.1.00523.S, 2017.1.00428.L, 2018.1.01359.S, 2019.1.00459.S, 2021.1.00280.L, 2021.1.00705.S, 2021.1.00225.S, 2023.1.00180.L
DC-709575	CRISTAL-14	**3045**, 5893	1727, 5893	9822, 13294, 13641, 13868, 16259, 16443, 17802	2017.1.00428.L, 2021.1.00280.L, 2021.1.00225.S
DC-742174	CRISTAL-17	**3045**, 5545, 5893, 6368	1727, 1837	9822/9999, 12328, 12440, 12461, 15647, 16443, 17802	2017.1.00428.L, 2021.1.00280.L, 2021.1.00225.S, 2023.1.00180.L
DC-842313	CRISTAL-01	**3045**, 4265	1727, 3954	9822, 13641, 13294, 14114, 14719, 16443, 17802	2012.1.00978.S, 2016.1.00171.S, 2016.1.00478.S, 2017.1.00428.L, 2019.1.01587.S, 2021.1.00280.L, 2022.1.00863.S
DC-848185	CRISTAL-02	**3045**	1727, 2417	9822, 12328, 13641, 13384, 14114, 16443, 17802	2011.0.00964.S, 2012.1.00523.S, 2013.1.01258.S, 2015.1.00928.S, 2015.1.00388.S, 2016.1.01149.S, 2017.1.00428.L, 2018.1.00348.S, 2019.1.00459.S, 2021.1.00280.L, 2021.1.00705.S
DC-873321	CRISTAL-07	**3045**, 5974	1727	9822, 13641, 16443, 17802	2012.1.00523.S, 2017.1.00428.L, 2021.1.00280.L, 2022.1.00863.S
DC-873756	CRISTAL-24	**3045**, 5974	1727	9822, 13641, 16259, 16443, 17802	2017.1.00428.L, 2019.1.00226.S, 2024.1.01401.S
VC-5100541407	CRISTAL-06	**3045**, 6480	1727	9822, 12578, 14495, 14596, 16443, 17802	2017.1.00428.L, 2021.1.00280.L
VC-5100822662	CRISTAL-04	**3045**, 5893	1727	9822, 12578, 13669, 14114, 16443, 17802	2017.1.00428.L, 2021.1.00280.L
VC-5100994794	CRISTAL-13	**3045**, 5893, 6368	1727, 1837	9822, 12328, 12440, 15647, 17802	2017.1.00428.L, 2021.1.00225.S, 2021.1.00280.L
VC-510128326	CRISTAL-25	**3045**, 5893	1727	9822, 15692, 16259, 16443, 17802	2015.1.00379.S, 2016.1.01546.S, 2017.1.00428.L, 2019.1.00226.S
VC-5101244930	CRISTAL-15	**3045**, 5893	1727, 1837	9822, 12328, 12440, 15100, 16443, 17802	2013.1.01292.S, 2017.1.00428.L, 2021.1.00280.L, 2021.1.00225.S
VC-5110377875	⋯	**3045**, 5893	1727	9822, 16259, 16443, 17802	2015.1.00379.S, 2017.1.00428.L, 2022.1.01118.S

Notes. Proposal IDs for JWST: 1727 (PI: Kartaltepe, NIRCam F115W/F150W/F277W/F444W, MIRI F770W), 1837 (PI: Dunlop, NIRCam F090W/F115W/F200W/F277W/F356W/F444W, MIRI F770W/F1800W), 1840 (PI: Alvarez-Marquez, NIRCam F115W/F150W/F200W/F250W/F335W/F444W), 2321 (PI: Best, NIRCam F212N/F200W/F444W/F470N), 2417 (PI: Riechers, NIRCam F200W/F356W/F444W, MIRI F1000W/F1500W/F2100W), 2514 (PI: Williams, NIRCam F115W/F150W/F200W/F277W/F356W/F444W), 3045 (this program, shown in bold; PI: Faisst, NIRSpec/IFU G235M/G395M), 3954 (PI: Lelli, MIRI F770W), 5545 (PI: Barrufet, NIRSpec Prism (MSA may not include source.)), 5893 (PI: Kakiichi, NIRCam/Grism F115W/F200W/F356W/F444W, MIRI F1000W/F2100W), 5974 (PI: Aravena, NIRSpec/IFU G395H), 6245 (PI: Gonzalez-Lopez, NIRCam F200W/F356W, NIRSpec G235M/G395H), 6368 (PI: Dickinson, NIRSpec/MSA Prism (MSA may not include source.)), 6480 (PI: Schouws, NIRCam/Grism, NIRCam F070W/F115W/F200W/F356W/F444W).
Proposal IDs for HST: 9822/9999 (PI: Scoville, ACS F814W), 12328 (PI: van Dokkum, ACS F814W, WFC3 F140W/G141/G800L), 12440 (PI: Faber, ACS F814W/F606W, WFC3 F125W/F160W), 12461 (PI: Riess, ACS F606W/F814W), 12578 (PI: Forster-Schreiber WFC3 F110W/F160W), 13294 (PI: Karim, ACS F814W), 13384 (PI: Riechers, ACS F606W, WFC3 F125W/F160W), 13641 (PI: Capak, WFC3 F105W/F125W/F160W), 13657 (PI: Kartaltepe, WFC3 F160W), 13669 (PI: Carollo WFC3 F438W), 13868 (PI: Kocevski, WFC3 F160W), 14114 (PI: van Dokkum, WFC3 F160W), 14495 (PI: Sobral, WFC3 F140W/G141), 14596 (PI: Fan, WFC3 F110W/F160W), 14719 (PI: Best, WFC3 F606W/F140W), 15100 (PI: Cooke, ACS F435W), 15647 (PI: Teplitz, ACS F435W, WFC3 F275W), 15692 (PI: Faisst, WFC3 F105W/F160W), 16259/16443 (PI: Momcheva, WFC3 F160W/G141), 16684 (PI: Lemaux, WFC3 F160W/G141), 17802 (PI: Kartaltepe, ACS F435W/F606W, WFC3 F098W).
Proposal IDs for ALMA: 2011.0.00964.S (PI: Riechers, Band 7), 2012.1.00523.S (PI: Capak, Band 7), 2012.1.00978.S (PI: Karim, Band 7), 2013.1.01258.S (PI: Riechers, Band 7), 2013.1.01292.S (PI: Leiton, Band 7), 2015.1.00379.S (PI: Schinnerer, Band 6), 2015.1.00388.S (PI: Lu, Band 6), 2015.1.00928.S (PI: Pavesi, Band 6), 2016.1.00171.S (PI: Daddi, Band 3), 2016.1.00478.S (PI: Miettinen, Band 7), 2016.1.01149.S (PI: Keating, Band 3), 2016.1.01546.S (PI: Cassata, Band 3), 2017.1.00428.L (ALPINE; PI: Le Fèvre, Band 7), 2018.1.00231.S (MORA; PI: Casey, Band 4), 2018.1.00348.S (PI: Faisst, Band 8), 2018.1.01359.S (PI: Aravena, Band 7), 2019.1.00226.S (PI: Ibar, Band 7), 2019.1.00459.S (PI: Scoville, Band 4), 2019.1.01587.S (TRICEPS; PI: Lelli, Band 7), 2021.1.00225.S (exMORA; PI: Casey, Band 4), 2021.1.00280.L (CRISTAL; PI: Herrera-Camus, Band 7), 2021.1.00705.S (PI: Cooper, Band 4), 2022.1.00863.S (PI: Hodge, Band 3), 2022.1.01118.S (PI: Béthermin, Band 7), 2023.1.00180.L (CHAMPS; PI: Faisst, Band 6), 2024.1.01401.S (PI: Herrera-Camus, Band 9).

Table A2
Summary of Physical Measurements

Name	M_*[a] ($10^9\,M_\odot$)	$\mathrm{SFR_{SED}}$[a] ($M_\odot\,\mathrm{yr}^{-1}$)	$\mathrm{SFR_{UV+IR}}$ ($M_\odot\,\mathrm{yr}^{-1}$)	$\mathrm{SFR_{[CII]}}$ ($M_\odot\,\mathrm{yr}^{-1}$)	$\mathrm{SFR_{H\alpha}}$ ($M_\odot\,\mathrm{yr}^{-1}$)	$\mathrm{SFR_{[OII]}}$ ($M_\odot\,\mathrm{yr}^{-1}$)	Age (Myr)	$E_s(B-V)$[b] (mag)	$E_n(B-V)$ (mag)	$12+\log(\mathrm{O/H})$[c]
DC-417567	$9.8^{+10.2}_{-5}$	72^{+42}_{-27}	72^{+11}_{-10}	23^{+5}_{-5}	73^{+4}_{-4}	35^{+4}_{-4}	105^{+100}_{-56}	$0.16^{+0.04}_{-0.04}$	$0.08^{+0.02}_{-0.02}$	$8.04^{+0.02}_{-0.02}$
DC-494763	$3.2^{+4.2}_{-1.8}$	28^{+36}_{-16}	27^{+21}_{-9}	39^{+5}_{-5}	57^{+4}_{-4}	42^{+5}_{-4}	175^{+352}_{-119}	$0.07^{+0.01}_{-0.01}$	$0.16^{+0.02}_{-0.02}$	$8.29^{+0.02}_{-0.02}$
DC-519281	$6.9^{+10.1}_{-4.1}$	32^{+35}_{-17}	31^{+17}_{-7}	43^{+11}_{-10}	131^{+11}_{-20}	50^{+15}_{-13}	324^{+331}_{-194}	$0.11^{+0.01}_{-0.01}$	$0.21^{+0.02}_{-0.04}$	$7.99^{+0.08}_{-0.08}$
DC-536534	$25.1^{+23.9}_{-12.2}$	62^{+64}_{-31}	35^{+22}_{-9}	69^{+17}_{-16}	404^{+30}_{-35}	234^{+37}_{-28}	456^{+275}_{-224}	$0.43^{+0.02}_{-0.02}$	$0.33^{+0.02}_{-0.03}$	$8.1^{+0.04}_{-0.05}$
DC-630594	$4.8^{+5.4}_{-2.5}$	37^{+39}_{-19}	25^{+11}_{-8}	52^{+6}_{-6}	68^{+16}_{-10}	68^{+37}_{-17}	186^{+227}_{-88}	$0.09^{+0.01}_{-0.01}$	$0.26^{+0.07}_{-0.05}$	$8.4^{+0.04}_{-0.04}$
DC-683613	$14.5^{+17.9}_{-8}$	68^{+67}_{-34}	38^{+16}_{-11}	70^{+7}_{-7}	40^{+4}_{-5}	34^{+8}_{-7}	274^{+271}_{-159}	$0.07^{+0.01}_{-0.01}$	$0.15^{+0.02}_{-0.04}$	$8.49^{+0.03}_{-0.05}$
DC-709575	$3.4^{+4.7}_{-2}$	28^{+39}_{-16}	>17	21^{+6}_{-5}	23^{+3}_{-3}	17^{+3}_{-3}	190^{+302}_{-95}	$0.06^{+0.01}_{-0.01}$	$0.15^{+0.04}_{-0.04}$	$8.27^{+0.02}_{-0.03}$
DC-742174	$3.2^{+4.9}_{-1.9}$	15^{+16}_{-8}	>19	9^{+3}_{-3}	15^{+2}_{-2}	4^{+1}_{-1}	354^{+338}_{-215}	$0.09^{+0.01}_{-0.01}$	$0.02^{+0.04}_{-0.04}$	$7.84^{+0.05}_{-0.05}$
DC-842313	$44.7^{+96.6}_{-30.5}$	204^{+918}_{-167}	>97	36^{+8}_{-7}	318^{+124}_{-85}	493^{+357}_{-179}	394^{+250}_{-221}	$0.25^{+0.02}_{-0.02}$	$0.64^{+0.11}_{-0.09}$	$8.48^{+0.03}_{-0.05}$
DC-848185	$20^{+18.1}_{-9.5}$	178^{+290}_{-110}	93^{+31}_{-18}	162^{+12}_{-11}	270^{+24}_{-15}	205^{+35}_{-26}	98^{+52}_{-48}	$0.15^{+0.01}_{-0.01}$	$0.2^{+0.03}_{-0.02}$	$8.28^{+0.02}_{-0.03}$
DC-873321	$10^{+11.4}_{-5.3}$	78^{+64}_{-35}	47^{+25}_{-14}	87^{+12}_{-12}	113^{+7}_{-10}	67^{+12}_{-18}	112^{+84}_{-63}	$0.13^{+0.01}_{-0.01}$	$0.2^{+0.02}_{-0.03}$	$8.11^{+0.06}_{-0.07}$
DC-873756	$33.9^{+6.9}_{-5.7}$	115^{+76}_{-46}	175^{+14}_{-10}	434^{+19}_{-19}	2^{+8}_{-1}	1^{+10}_{-0}	550^{+317}_{-169}	$0.43^{+0.02}_{-0.02}$	>-0.14	$8.68^{+0.58}_{-0.88}$
VC-5100541407	$12.3^{+12.2}_{-6.1}$	42^{+50}_{-23}	45^{+9}_{-6}	112^{+14}_{-13}	5^{+14}_{-3}	1^{+12}_{-1}	400^{+427}_{-239}	$0.1^{+0.02}_{-0.02}$	$0.11^{+0}_{-0.79}$	$8.21^{+0.24}_{-0.4}$
VC-5100822662	$14.1^{+13.4}_{-6.9}$	78^{+48}_{-30}	42^{+8}_{-7}	69^{+7}_{-7}	68^{+15}_{-11}	56^{+21}_{-14}	237^{+196}_{-122}	$0.06^{+0.01}_{-0.01}$	$0.19^{+0.05}_{-0.05}$	$8.33^{+0.04}_{-0.04}$
VC-5100994794	$4.5^{+5.3}_{-2.4}$	32^{+51}_{-20}	30^{+10}_{-8}	45^{+5}_{-5}	78^{+22}_{-22}	74^{+35}_{-33}	193^{+252}_{-95}	$0.09^{+0.01}_{-0.01}$	$0.3^{+0.08}_{-0.11}$	$8.41^{+0.04}_{-0.05}$
VC-5101218326	$79.4^{+86.5}_{-41.4}$	562^{+534}_{-274}	83^{+14}_{-7}	190^{+10}_{-10}	11^{+28}_{-7}	5^{+27}_{-4}	646^{+97}_{-275}	$0.16^{+0.01}_{-0.01}$	$0.1^{+0}_{-0.69}$	$8.36^{+0.34}_{-0.3}$
VC-5101244930	$4.9^{+5.6}_{-2.6}$	28^{+20}_{-12}	>26	41^{+11}_{-10}	75^{+22}_{-11}	55^{+38}_{-19}	183^{+365}_{-88}	0.03^{+0}_{-0}	$0.24^{+0.08}_{-0.06}$	$8.24^{+0.1}_{-0.13}$
VC-5110377875	$14.7^{+6.8}_{-4.7}$	99^{+75}_{-43}	>85	176^{+13}_{-13}	92^{+40}_{-31}	93^{+70}_{-51}	161^{+127}_{-108}	$0.11^{+0.01}_{-0.01}$	$0.26^{+0.12}_{-0.14}$	$8.41^{+0.08}_{-0.09}$

Notes.
[a] From R. Herrera-Camus et al. (2025) based on CIGALE fits in I. Mitsuhashi et al. (2024).
[b] From A. Tsujita et al. (2025).
[c] Uses the R. L. Sanders et al. (2024) strong-line calibration.

Table A3
Summary of Measured (Dust-corrected) Line Ratios

Name	$\log(R_{23})$	$\log(R_3)$	$\log(R_2)$	$\log(O_{32})$	$\log(N_2)$	$\log(S_2)$	$\log(S_R)$
DC-417567	$1.03^{+0.01}_{-0.01}$	$0.97^{+0.01}_{-0.01}$	$0.14^{+0.02}_{-0.03}$	$0.71^{+0.02}_{-0.02}$	$-1.13^{+0.06}_{-0.03}$	$-1.25^{+0.06}_{-0.06}$	$0.11^{+0.10}_{-0.06}$
DC-494763	$0.95^{+0.01}_{-0.01}$	$0.83^{+0.01}_{-0.01}$	$0.33^{+0.03}_{-0.03}$	$0.37^{+0.02}_{-0.03}$	$-0.93^{+0.02}_{-0.03}$	$-0.95^{+0.03}_{-0.05}$	$-0.22^{+0.07}_{-0.07}$
DC-519281	$0.95^{+0.01}_{-0.02}$	$0.89^{+0.01}_{-0.01}$	$0.04^{+0.09}_{-0.09}$	$0.73^{+0.08}_{-0.09}$	$-0.97^{+0.10}_{-0.05}$	$-1.11^{+0.09}_{-0.12}$	$-0.01^{+0.13}_{-0.11}$
DC-536534	$1.06^{+0.01}_{-0.01}$	$0.99^{+0.01}_{-0.01}$	$0.23^{+0.04}_{-0.06}$	$0.64^{+0.05}_{-0.05}$	$-1.01^{+0.08}_{-0.11}$	$-1.29^{+0.13}_{-0.06}$	$-0.20^{+0.12}_{-0.15}$
DC-630594	$0.99^{+0.05}_{-0.03}$	$0.84^{+0.03}_{-0.03}$	$0.46^{+0.07}_{-0.06}$	$0.24^{+0.04}_{-0.04}$	$-0.93^{+0.03}_{-0.01}$	$-0.91^{+0.02}_{-0.02}$	$-0.12^{+0.02}_{-0.03}$
DC-683613	$0.82^{+0.03}_{-0.03}$	$0.62^{+0.02}_{-0.01}$	$0.39^{+0.05}_{-0.05}$	$0.10^{+0.05}_{-0.03}$	$-0.76^{+0.04}_{-0.03}$	$-0.83^{+0.07}_{-0.03}$	$-0.05^{+0.05}_{-0.10}$
DC-709575	$0.99^{+0.02}_{-0.02}$	$0.88^{+0.02}_{-0.02}$	$0.34^{+0.03}_{-0.04}$	$0.42^{+0.03}_{-0.02}$	$-1.16^{+0.05}_{-0.04}$	$-1.01^{+0.04}_{-0.05}$	$-0.06^{+0.09}_{-0.04}$
DC-742174	$0.96^{+0.02}_{-0.02}$	$0.92^{+0.02}_{-0.02}$	$-0.11^{+0.06}_{-0.05}$	$0.91^{+0.03}_{-0.05}$	$-1.61^{+0.29}_{-0.04}$	$-1.10^{+0.07}_{-0.04}$	$-0.12^{+0.11}_{-0.15}$
DC-842313	$1.12^{+0.06}_{-0.04}$	$0.94^{+0.03}_{-0.04}$	$0.65^{+0.10}_{-0.08}$	$0.14^{+0.07}_{-0.05}$	$-0.75^{+0.04}_{-0.41}$	$-0.64^{+0.03}_{-0.14}$	$-0.13^{+0.02}_{-0.02}$
DC-848185	$0.97^{+0.02}_{-0.01}$	$0.86^{+0.01}_{-0.01}$	$0.34^{+0.03}_{-0.04}$	$0.39^{+0.04}_{-0.02}$	$-0.75^{+0.09}_{-0.08}$	$-0.70^{+0.07}_{-0.08}$	$-0.07^{+0.02}_{-0.03}$
DC-873321	$1.04^{+0.02}_{-0.02}$	$0.96^{+0.01}_{-0.01}$	$0.22^{+0.07}_{-0.09}$	$0.62^{+0.08}_{-0.07}$	$-1.08^{+0.04}_{-0.06}$	$-1.16^{+0.06}_{-0.04}$	$-0.04^{+0.04}_{-0.05}$
DC-873756	$0.54^{+0.44}_{-0.27}$	$0.19^{+0.37}_{-0.21}$	$-0.12^{+0.70}_{-0.44}$	$-0.10^{+0.60}_{-0.72}$	$-0.25^{+0.27}_{-0.18}$	$-0.33^{+0.34}_{-0.10}$	$-0.02^{+0.17}_{-0.16}$
VC-5100541407	$0.52^{+0.35}_{-0.13}$	$0.42^{+0.23}_{-0.14}$	$-0.02^{+0.40}_{-0.42}$	$0.36^{+0.22}_{-0.21}$	$-0.77^{+0.09}_{-0.11}$	$-0.63^{+0.08}_{-0.16}$	$-0.14^{+0.08}_{-0.25}$
VC-5100822662	$0.95^{+0.03}_{-0.04}$	$0.82^{+0.02}_{-0.03}$	$0.37^{+0.06}_{-0.06}$	$0.33^{+0.05}_{-0.04}$	$-0.97^{+0.07}_{-0.05}$	$-0.98^{+0.09}_{-0.03}$	$-0.09^{+0.03}_{-0.04}$
VC-5100994794	$0.94^{+0.03}_{-0.07}$	$0.77^{+0.03}_{-0.05}$	$0.43^{+0.07}_{-0.10}$	$0.22^{+0.06}_{-0.05}$	$-0.96^{+0.03}_{-0.02}$	$-0.89^{+0.03}_{-0.02}$	$0.03^{+0.03}_{-0.05}$
VC-5101218326	$0.64^{+0.19}_{-0.17}$	$0.45^{+0.21}_{-0.11}$	$0.07^{+0.37}_{-0.27}$	$0.23^{+0.29}_{-0.36}$	$-0.64^{+0.21}_{-0.16}$	$-0.46^{+0.12}_{-0.17}$	$0.01^{+0.13}_{-0.14}$
VC-5101244930	$1.01^{+0.06}_{-0.04}$	$0.90^{+0.03}_{-0.03}$	$0.32^{+0.13}_{-0.18}$	$0.46^{+0.13}_{-0.12}$	$-1.19^{+0.11}_{-0.06}$	$-0.87^{+0.04}_{-0.05}$	$-0.21^{+0.04}_{-0.05}$
VC-5110377875	$0.94^{+0.07}_{-0.10}$	$0.78^{+0.05}_{-0.07}$	$0.44^{+0.13}_{-0.15}$	$0.23^{+0.09}_{-0.09}$	$-1.09^{+0.06}_{-0.04}$	$-0.98^{+0.05}_{-0.05}$	$0.00^{+0.07}_{-0.07}$

Note. Definition of line ratios: $R_{23} \equiv$ ([O III]$_{5007}$ + [O III]$_{4959}$ + [O II]$_{3727}$)/Hβ, $R_3 \equiv$ ([O III]$_{5007}$ + [O III]$_{4959}$)/Hβ, $R_2 \equiv$ [O II]$_{3727}$/Hβ, $O_{32} \equiv$ [O III]$_{5007}$/[O II]$_{3727}$, $N_2 \equiv$ [N II]$_{6585}$/Hα, $S_2 \equiv$ ([S II]$_{6732}$ + [S II]$_{6718}$)/Hα, $S_R \equiv$ [S II]$_{6732}$/[S II]$_{6718}$. Note that [O II] includes the doublet, which is unresolved.

Table A4
Observed Emission-line Fluxes in 10^{-18} erg s^{-1} cm^{-2}

Name	[O II][a]	[Ne III]$_{3868}$	Hγ	[O III]$_{4363}$	Hβ	[O III]$_{4959}$	[O III]$_{5007}$	[N II]$_{6548}$	Hα		[N II]$_{6585}$	[S II]$_{6718}$	[S II]$_{6732}$	[O II]$_{7322}$	[O II]$_{7332}$
									(total)	(broad)					
DC-417567	$14.46^{+0.38}_{-0.46}$	$5.53^{+0.36}_{-0.32}$	$5.14^{+0.21}_{-0.27}$	$1.82^{+0.42}_{-0.32}$	$11.51^{+0.21}_{-0.26}$	$26.93^{+0.25}_{-0.24}$	$81.28^{+0.31}_{-0.29}$	$0.90^{+0.13}_{-0.06}$	$36.25^{+0.13}_{-0.36}$	⋯	$2.69^{+0.38}_{-0.17}$	$0.90^{+0.16}_{-0.16}$	$1.18^{+0.18}_{-0.16}$	$0.59^{+0.29}_{-0.21}$	$0.59^{+0.16}_{-0.15}$
DC-494763	$13.54^{+0.71}_{-0.30}$	$2.76^{+0.41}_{-0.51}$	$3.46^{+0.43}_{-0.31}$	$0.88^{+0.50}_{-0.41}$	$7.66^{+0.18}_{-0.18}$	$13.43^{+0.19}_{-0.14}$	$39.44^{+0.22}_{-0.24}$	$1.02^{+0.05}_{-0.07}$	$26.42^{+0.28}_{-0.24}$	⋯	$3.06^{+0.14}_{-0.21}$	$1.87^{+0.13}_{-0.18}$	$1.12^{+0.19}_{-0.15}$	<0.48	$0.32^{+0.13}_{-0.12}$
DC-519281	$11.02^{+2.38}_{-2.18}$	$4.73^{+1.56}_{-1.82}$	$3.99^{+0.93}_{-2.12}$	$5.54^{+2.16}_{-2.43}$	$12.55^{+0.34}_{-0.33}$	$24.95^{+0.31}_{-0.37}$	$74.96^{+0.45}_{-0.42}$	$1.20^{+0.42}_{-0.14}$	$45.87^{+0.80}_{-1.51}$	$12.35^{+1.93}_{-0.97}$	$3.61^{+1.25}_{-0.41}$	$1.35^{+0.47}_{-0.26}$	$1.32^{+0.33}_{-0.28}$	<1.19	<0.85
DC-536534	$24.97^{+2.44}_{-2.54}$	$9.51^{+1.09}_{-1.12}$	$11.03^{+0.81}_{-0.43}$	$3.94^{+1.16}_{-1.08}$	$22.02^{+0.41}_{-0.58}$	$56.18^{+0.42}_{-0.62}$	$167.58^{+0.62}_{-0.58}$	$1.89^{+0.28}_{-0.36}$	$92.32^{+1.63}_{-1.26}$	$34.45^{+5.48}_{-3.10}$	$5.68^{+0.83}_{-1.07}$	$1.92^{+0.32}_{-0.34}$	$1.23^{+0.33}_{-0.32}$	$0.83^{+0.42}_{-0.26}$	$0.75^{+0.51}_{-0.38}$
DC-630594	$18.55^{+0.64}_{-0.90}$	$2.82^{+0.72}_{-0.60}$	$3.32^{+0.47}_{-0.49}$	$0.83^{+0.44}_{-0.43}$	$8.81^{+0.55}_{-0.73}$	$16.13^{+0.66}_{-0.41}$	$45.68^{+0.66}_{-0.49}$	$1.37^{+0.10}_{-0.05}$	$34.31^{+0.22}_{-0.24}$	⋯	$4.10^{+0.29}_{-0.14}$	$2.46^{+0.16}_{-0.16}$	$1.84^{+0.13}_{-0.10}$	$0.36^{+0.13}_{-0.18}$	$0.72^{+0.26}_{-0.24}$
DC-683613	$10.31^{+0.97}_{-0.90}$	< 2.03	$2.31^{+0.65}_{-0.57}$	$1.70^{+0.84}_{-1.10}$	$5.02^{+0.13}_{-0.24}$	$5.34^{+0.10}_{-0.16}$	$15.94^{+0.21}_{-0.15}$	$0.85^{+0.07}_{-0.05}$	$17.13^{+0.37}_{-0.65}$	$2.80^{+1.02}_{-0.69}$	$2.55^{+0.22}_{-0.16}$	$1.21^{+0.13}_{-0.15}$	$1.04^{+0.12}_{-0.13}$	<0.49	$0.42^{+0.15}_{-0.13}$
DC-709575	$8.97^{+0.24}_{-0.37}$	$1.65^{+0.17}_{-0.15}$	$1.79^{+0.22}_{-0.10}$	$0.74^{+0.23}_{-0.13}$	$4.89^{+0.16}_{-0.21}$	$9.39^{+0.16}_{-0.15}$	$28.37^{+0.24}_{-0.21}$	$0.39^{+0.04}_{-0.04}$	$16.67^{+0.17}_{-0.15}$	⋯	$1.16^{+0.12}_{-0.13}$	$0.87^{+0.13}_{-0.12}$	$0.78^{+0.08}_{-0.09}$	<0.26	$0.22^{+0.07}_{-0.06}$
DC-742174	$2.41^{+0.27}_{-0.22}$	$1.87^{+0.18}_{-0.13}$	$1.33^{+0.15}_{-0.17}$	< 10.27	$3.19^{+0.15}_{-0.13}$	$6.59^{+0.17}_{-0.11}$	$19.90^{+0.20}_{-0.14}$	< 0.23	$9.36^{+0.11}_{-0.18}$	⋯	<0.69	$0.42^{+0.09}_{-0.09}$	$0.33^{+0.06}_{-0.08}$	<0.18	$0.34^{+0.14}_{-0.09}$
DC-842313	$16.63^{+0.90}_{-1.28}$	$3.62^{+1.32}_{-0.79}$	$3.46^{+0.64}_{-0.67}$	$1.79^{+0.48}_{-0.77}$	$7.67^{+0.67}_{-0.77}$	$17.54^{+0.58}_{-0.91}$	$53.38^{+0.93}_{-1.26}$	$1.29^{+0.12}_{-0.57}$	$45.46^{+3.61}_{-0.53}$	$22.25^{+1.86}_{-3.84}$	$3.87^{+0.36}_{-1.72}$	$3.13^{+0.11}_{-0.11}$	$2.38^{+0.11}_{-0.14}$	$0.50^{+0.39}_{-0.21}$	$0.79^{+0.46}_{-0.14}$
DC-848185	$53.08^{+2.75}_{-2.72}$	$9.91^{+2.44}_{-1.45}$	$13.63^{+1.44}_{-2.36}$	$2.62^{+1.93}_{-1.02}$	$30.85^{+0.53}_{-0.96}$	$56.71^{+0.66}_{-0.40}$	$169.74^{+0.91}_{-0.68}$	$4.05^{+0.12}_{-0.12}$	$111.18^{+0.71}_{-1.02}$	$44.77^{+9.87}_{-11.36}$	$12.16^{+0.36}_{-0.37}$	$7.51^{+0.37}_{-0.42}$	$6.27^{+0.42}_{-0.30}$	$1.60^{+0.30}_{-0.32}$	$0.79^{+0.26}_{-0.11}$
DC-873321	$18.01^{+3.61}_{-2.64}$	$6.52^{+1.59}_{-0.87}$	$6.17^{+1.43}_{-1.07}$	< 6.79	$13.72^{+0.37}_{-0.36}$	$31.97^{+0.31}_{-0.24}$	$96.64^{+0.51}_{-0.41}$	$1.08^{+0.09}_{-0.08}$	$49.37^{+0.35}_{-0.46}$	$10.11^{+2.46}_{-3.62}$	$3.25^{+0.26}_{-0.24}$	$1.51^{+0.11}_{-0.20}$	$1.36^{+0.14}_{-0.14}$	$0.76^{+0.19}_{-0.17}$	$0.25^{+0.16}_{-0.17}$
DC-873756	$18.75^{+12.14}_{-6.10}$	< 18.61	< 16.98	< 15.99	$11.18^{+6.09}_{-5.88}$	< 19.72	$10.10^{+4.83}_{-7.29}$	$2.64^{+1.14}_{-0.72}$	< 11.95	⋯	$7.93^{+3.43}_{-2.15}$	$4.13^{+1.58}_{-1.47}$	$3.40^{+1.38}_{-1.04}$	<6.58	<5.71
VC-5100541407	$9.03^{+2.81}_{-2.93}$	< 9.17	< 6.96	< 6.08	$6.92^{+3.59}_{-2.71}$	$4.43^{+1.33}_{-1.35}$	$14.54^{+1.96}_{-2.84}$	$0.74^{+0.19}_{-0.15}$	$13.61^{+1.08}_{-0.69}$	⋯	$2.22^{+0.56}_{-0.46}$	$1.87^{+0.37}_{-0.54}$	$1.22^{+0.37}_{-0.39}$	<1.08	$0.78^{+0.39}_{-0.29}$
VC-5100822662	$21.71^{+1.18}_{-1.18}$	$4.54^{+1.24}_{-1.06}$	$4.74^{+0.76}_{-0.38}$	$1.11^{+0.51}_{-0.54}$	$11.65^{+0.70}_{-0.61}$	$19.09^{+0.99}_{-0.59}$	$59.57^{+1.15}_{-0.81}$	$1.32^{+0.23}_{-0.19}$	$41.13^{+2.58}_{-0.92}$	⋯	$3.97^{+0.68}_{-0.57}$	$2.23^{+0.09}_{-0.08}$	$1.78^{+0.12}_{-0.15}$	$0.25^{+0.08}_{-0.08}$	$0.14^{+0.08}_{-0.08}$
VC-5100994794	$14.85^{+1.14}_{-0.98}$	$4.10^{+1.32}_{-1.22}$	$2.41^{+0.60}_{-0.48}$	< 1.34	$7.97^{+1.10}_{-0.68}$	$11.77^{+0.61}_{-0.74}$	$36.88^{+0.92}_{-0.80}$	$1.21^{+0.07}_{-0.05}$	$32.59^{+0.21}_{-0.21}$	⋯	$3.63^{+0.21}_{-0.16}$	$2.08^{+0.21}_{-0.12}$	$2.22^{+0.08}_{-0.14}$	$0.71^{+0.11}_{-0.18}$	$0.58^{+0.19}_{-0.12}$
VC-5101218326	$23.93^{+5.92}_{-6.54}$	< 19.23	< 16.31	< 13.56	$14.14^{+4.64}_{-5.46}$	$10.39^{+3.47}_{-2.23}$	$24.35^{+8.38}_{-5.44}$	$2.20^{+0.86}_{-0.78}$	$26.78^{+3.73}_{-2.42}$	⋯	$6.61^{+2.58}_{-2.34}$	$3.57^{+2.54}_{-1.00}$	$3.61^{+1.11}_{-0.55}$	<5.32	<6.01
VC-5101244930	$16.47^{+2.89}_{-5.07}$	$4.20^{+1.17}_{-0.83}$	$4.86^{+0.56}_{-0.76}$	< 2.09	$10.02^{+0.78}_{-0.82}$	$21.21^{+0.78}_{-0.85}$	$61.55^{+1.15}_{-1.47}$	$0.63^{+0.11}_{-0.06}$	$38.33^{+0.21}_{-0.39}$	$9.33^{+3.10}_{-1.89}$	$1.88^{+0.34}_{-0.17}$	$2.41^{+0.13}_{-0.17}$	$1.49^{+0.15}_{-0.19}$	$0.57^{+0.12}_{-0.12}$	$0.52^{+0.19}_{-0.10}$
VC-5110377875	$23.83^{+2.07}_{-2.33}$	$6.27^{+2.94}_{-2.57}$	$4.87^{+1.56}_{-0.72}$	< 11.26	$11.81^{+2.03}_{-1.53}$	$16.78^{+1.50}_{-1.23}$	$55.06^{+2.19}_{-2.48}$	$1.17^{+0.21}_{-0.13}$	$45.48^{+1.38}_{-0.68}$	⋯	$3.51^{+0.64}_{-0.39}$	$2.32^{+0.27}_{-0.27}$	$2.35^{+0.34}_{-0.31}$	$0.77^{+0.27}_{-0.16}$	$0.72^{+0.43}_{-0.31}$

Note. Limits are 3σ.
[a] The [O II] doublet is not resolved.

Appendix B
Individual Galaxies

Figure B1 displays various data taken by JWST, HST, and ALMA for each of the 18 ALPINE-CRISTAL-JWST survey targets.

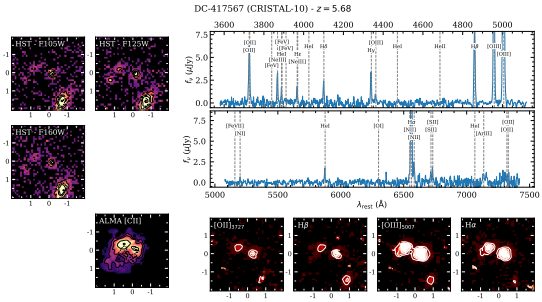

Figure B1. Summary figure for target DC-417567. Left six panels: JWST/NIRCam and MIRI (if available) images (or HST for DC-417567) with corresponding contours (solid black) overlaid. The ALMA [C II] moment map with [C II] (solid black) and far-IR continuum (dashed black) emission contours overlaid. Lower right four panels: Emission-line maps ([O II], Hβ, [O III], and Hα from left to right). Large panels: NIRSpec IFU integrated continuum-subtracted optical spectra with some emission line indicated. All cutout images are $4'' \times 4''$ in size and contours show 3σ, 5σ, 10σ, 15σ, 30σ, 50σ, and 100σ levels.

(The complete figure set (18 images) is available in the online article.)

ORCID iDs

A. L. Faisst https://orcid.org/0000-0002-9382-9832
S. Fujimoto https://orcid.org/0000-0001-7201-5066
A. Tsujita https://orcid.org/0000-0002-0498-5041
W. Wang https://orcid.org/0000-0002-7964-6749
N. Nezhad https://orcid.org/0000-0002-7755-8649
F. Loiacono https://orcid.org/0000-0002-8858-6784
H. Übler https://orcid.org/0000-0003-4891-0794
M. Béthermin https://orcid.org/0000-0002-3915-2015
P. Cassata https://orcid.org/0000-0002-6716-4400
M. Dessauges-Zavadsky https://orcid.org/0000-0003-0348-2917
R. Herrera-Camus https://orcid.org/0000-0002-2775-0595
D. Schaerer https://orcid.org/0000-0001-7144-7182
J. D. Silverman https://orcid.org/0000-0002-0000-6977
L. Yan https://orcid.org/0000-0003-1710-9339
M. Aravena https://orcid.org/0000-0002-6290-3198
I. De Looze https://orcid.org/0000-0001-9419-6355
N. M. Förster Schreiber https://orcid.org/0000-0003-4264-3381
J. Spilker https://orcid.org/0000-0003-3256-5615
K. Tadaki https://orcid.org/0000-0001-9728-8909
C. M. Casey https://orcid.org/0000-0002-0930-6466
M. Franco https://orcid.org/0000-0002-3560-8599
S. Harish https://orcid.org/0000-0003-0129-2079
H. J. McCracken https://orcid.org/0000-0002-9489-7765
J. S. Kartaltepe https://orcid.org/0000-0001-9187-3605
A. M. Koekemoer https://orcid.org/0000-0002-6610-2048
A. A. Khostovan https://orcid.org/0000-0002-0101-336X
D. Liu https://orcid.org/0000-0001-9773-7479
J. Rhodes https://orcid.org/0000-0002-4485-8549
B. E. Robertson https://orcid.org/0000-0002-4271-0364
R. Amorin https://orcid.org/0000-0001-5758-1000
R. J. Assef https://orcid.org/0000-0002-9508-3667
A. J. Battisti https://orcid.org/0000-0003-4569-2285
J. E. Birkin https://orcid.org/0000-0002-3272-7568
M. Boquien https://orcid.org/0000-0003-0946-6176
E. Da Cunha https://orcid.org/0000-0001-9759-4797
P. Dam https://orcid.org/0009-0007-7842-9930
R. L. Davies https://orcid.org/0000-0002-3324-4824
D. A. Gómez-Espinoza https://orcid.org/0009-0008-1835-7557
A. Ferrara https://orcid.org/0000-0002-9400-7312
Y. Fudamoto https://orcid.org/0000-0001-7440-8832
S. Gillman https://orcid.org/0000-0001-9885-4589
M. Ginolfi https://orcid.org/0000-0002-9122-1700
G. Gozaliasl https://orcid.org/0000-0002-0236-919X
C. Gruppioni https://orcid.org/0000-0002-5836-4056
A. Hadi https://orcid.org/0009-0003-3097-6733
N. Hathi https://orcid.org/0000-0001-6145-5090
E. Ibar https://orcid.org/0009-0008-9801-2224
R. Ikeda https://orcid.org/0000-0002-2634-9169
H. Inami https://orcid.org/0000-0003-4268-0393
G. C. Jones https://orcid.org/0000-0002-0267-9024
M. Kohandel https://orcid.org/0000-0003-1041-7865
Y.-H. Lin https://orcid.org/0000-0001-8792-3091
Z. Liu https://orcid.org/0000-0002-9252-114X
L.-J. Liu https://orcid.org/0009-0004-1270-2373
A. S. Long https://orcid.org/0000-0002-7530-8857
G. Magdis https://orcid.org/0000-0002-4872-2294
C. Maraston https://orcid.org/0000-0001-7711-3677
C. L. Martin https://orcid.org/0000-0001-9189-7818
I. Mitsuhashi https://orcid.org/0000-0001-7300-9450
B. Mobasher https://orcid.org/0000-0001-5846-4404
J. Molina https://orcid.org/0000-0002-8136-8127
A. Nanni https://orcid.org/0000-0001-2345-6789
M. Palla https://orcid.org/0000-0002-3574-9578
A. Pallottini https://orcid.org/0000-0002-7129-5761
F. Pozzi https://orcid.org/0000-0002-7412-647X
M. Relano https://orcid.org/0000-0003-1682-1148
W. Ren https://orcid.org/0000-0002-3742-6609
D. A. Riechers https://orcid.org/0000-0001-9585-1462
M. Romano https://orcid.org/0000-0002-9948-3916
D. B. Sanders https://orcid.org/0000-0002-1233-9998
P. Sawant https://orcid.org/0000-0002-0498-8074
M. Shuntov https://orcid.org/0000-0002-7087-0701
R. Smit https://orcid.org/0000-0001-8034-7802
L. Sommovigo https://orcid.org/0000-0002-2906-2200
M. Talia https://orcid.org/0000-0003-4352-2063
L. Vallini https://orcid.org/0000-0002-3258-3672
E. Veraldi https://orcid.org/0009-0007-1304-7771
D. Vergani https://orcid.org/0000-0003-0898-2216
A. P. Vijayan https://orcid.org/0000-0002-1905-4194
V. Villanueva https://orcid.org/0000-0002-5877-379X
G. Zamorani https://orcid.org/0000-0002-2318-301X

References

Abazajian, K. N., Adelman-McCarthy, J. K., Agüeros, M. A., et al. 2009, ApJS, 182, 543
Accard, C., et al. 2025, ApJ, submitted (arXiv:2508.13136)
Allende Prieto, C., Lambert, D. L., & Asplund, M. 2001, ApJL, 556, L63
Astropy Collaboration, Price-Whelan, A. M., Lim, P. L., et al. 2022, ApJ, 935, 167
Astropy Collaboration, Price-Whelan, A. M., Sipőcz, B. M., et al. 2018, AJ, 156, 123
Astropy Collaboration, Robitaille, T. P., Tollerud, E. J., et al. 2013, A&A, 558, A33
Atek, H., Kunth, D., Schaerer, D., et al. 2009, A&A, 506, L1

Backhaus, B. E., Cleri, N. J., Trump, J. R., et al. 2025, arXiv:2502.03519
Baldwin, J. A., Phillips, M. M., & Terlevich, R. 1981, PASP, 93, 5
Battisti, A. J., Bagley, M. B., Baronchelli, I., et al. 2022, MNRAS, 513, 4431
Bergemann, M., Hoppe, R., Semenova, E., et al. 2021, MNRAS, 508, 2236
Béthermin, M., Accard, C., Guillaume, C., et al. 2023, A&A, 680, L8
Béthermin, M., Fudamoto, Y., Ginolfi, M., et al. 2020, A&A, 643, A2
Birkin, J. E., Hutchison, T. A., Welch, B., et al. 2023, ApJ, 958, 64
Birkin, J. E., Spilker, J. S., Herrera-Camus, R., et al. 2025, ApJ, 985, 243
Boquien, M., Burgarella, D., Roehlly, Y., et al. 2019, A&A, 622, A103
Bouwens, R. J., Illingworth, G. D., Oesch, P. A., et al. 2015, ApJ, 803, 34
Bouwens, R. J., Smit, R., Schouws, S., et al. 2022, ApJ, 931, 160
Brammer, G. B., van Dokkum, P. G., Franx, M., et al. 2012, ApJS, 200, 13
Brinchmann, J., Charlot, S., White, S. D. M., et al. 2004, MNRAS, 351, 1151
Burgarella, D., Buat, V., & Iglesias-Páramo, J. 2005, MNRAS, 360, 1413
Calzetti, D. 2001, PASP, 113, 1449
Calzetti, D., Armus, L., Bohlin, R. C., et al. 2000, ApJ, 533, 682
Capak, P. L., Carilli, C., Jones, G., et al. 2015, Natur, 522, 455
Caputi, K. I., Deshmukh, S., Ashby, M. L. N., et al. 2017, ApJ, 849, 45
Cardelli, J. A., Clayton, G. C., & Mathis, J. S. 1989, ApJ, 345, 245
Carnall, A. C., McLure, R. J., Dunlop, J. S., & Davé, R. 2018, MNRAS, 480, 4379
Carnall, A. C., McLure, R. J., Dunlop, J. S., et al. 2019, MNRAS, 490, 417
Carniani, S., Ferrara, A., Maiolino, R., et al. 2020, MNRAS, 499, 5136
CASA Team, Bean, B., Bhatnagar, S., et al. 2022, PASP, 134, 114501
Casey, C. M., Kartaltepe, J. S., Drakos, N. E., et al. 2023, ApJ, 954, 31
Chabrier, G. 2003, PASP, 115, 763
Choban, C. R., Kereš, D., Sandstrom, K. M., et al. 2024, MNRAS, 529, 2356
Clarke, L., Shapley, A. E., Sanders, R. L., et al. 2024, ApJ, 977, 133
Cole, J., & Papovich, C. 2023, AAS Meeting, 241, 412.05
Cole, J. W., Papovich, C., Finkelstein, S. L., et al. 2025, ApJ, 979, 193
COSMOS Project 2020, Cosmic Evolution Survey with HST (COSMOS), IPAC, doi:10.26131/IRSA178
Curti, M., D'Eugenio, F., Carniani, S., et al. 2023, MNRAS, 518, 425
Cutler, S. E., Whitaker, K. E., Mowla, L. A., et al. 2022, ApJ, 925, 34
da Cunha, E., Charlot, S., & Elbaz, D. 2008, MNRAS, 388, 1595
da Cunha, E., Walter, F., Smail, I. R., et al. 2015, ApJ, 806, 110
Daddi, E., Dickinson, M., Morrison, G., et al. 2007, ApJ, 670, 156
Danhaive, A. L., Tacchella, S., Übler, H., et al. 2025, MNRAS, 543, 3249
Davé, R., Finlator, K., & Oppenheimer, B. D. 2012, MNRAS, 421, 98
Davidzon, I., Ilbert, O., Laigle, C., et al. 2017, A&A, 605, A70
Davies, R. L., Förster Schreiber, N. M., Übler, H., et al. 2019, ApJ, 873, 122
Dayal, P., & Ferrara, A. 2018, PhR., 780, 1
Dayal, P., Ferrara, A., & Dunlop, J. S. 2013, MNRAS, 430, 2891
De Looze, I., Baes, M., Bendo, G. J., Cortese, L., & Fritz, J. 2011, MNRAS, 416, 2712
De Lucia, G., Muzzin, A., & Weinmann, S. 2014, NewAR, 62, 1
Dessauges-Zavadsky, M., Ginolfi, M., Pozzi, F., et al. 2020, A&A, 643, A5
Devereaux, T., Cassata, P., Ibar, E., et al. 2024, A&A, 686, A156
Eisenstein, D. J., Willott, C., Alberts, S., et al. 2023, arXiv:2306.02465
Endsley, R., Chisholm, J., Stark, D. P., Topping, M. W., & Whitler, L. 2025, ApJ, 987, 189
Faisst, A. L., Capak, P. L., Emami, N., Tacchella, S., & Larson, K. L. 2019, ApJ, 884, 133
Faisst, A. L., Capak, P. L., Yan, L., et al. 2017, ApJ, 847, 21
Faisst, A. L., Liu, L.-J., Dubois, Y., et al. 2025, arXiv:2510.16106
Faisst, A. L., Masters, D., Wang, Y., et al. 2018, ApJ, 855, 132
Faisst, A. L., Schaerer, D., Lemaux, B. C., et al. 2020, ApJS, 247, 61
Faisst, A. L., Yan, L., Béthermin, M., et al. 2022, Univ, 8, 314
Feldmann, R. 2015, MNRAS, 449, 3274
Feltre, A., Charlot, S., & Gutkin, J. 2016, MNRAS, 456, 3354
Ferrara, A., & Peroux, C. 2021, MNRAS, 503, 4537
Finkelstein, S. L., Bagley, M. B., Arrabal Haro, P., et al. 2025, ApJL, 983, L4
Fisher, R., Bowler, R. A. A., Stefanon, M., et al. 2025, MNRAS, 539, 109
Förster Schreiber, N. M., Genzel, R., Bouché, N., et al. 2009, ApJ, 706, 1364
Förster Schreiber, N. M., Renzini, A., Mancini, C., et al. 2018, ApJS, 238, 21
Förster Schreiber, N. M., Übler, H., Davies, R. L., et al. 2019, ApJ, 875, 21
Franco, M., Casey, C. M., Koekemoer, A. M., et al. 2025, arXiv:2506.03256
Fujimoto, S., Faisst, A. L., Tsujita, A., et al. 2025, arXiv:2510.16116
Fujimoto, S., Ouchi, M., Ferrara, A., et al. 2019, ApJ, 887, 107
Gaia Collaboration, Vallenari, A., Brown, A. G. A., et al. 2023, A&A, 674, A1
Gallerani, S., Pallottini, A., Feruglio, C., et al. 2018, MNRAS, 473, 1909
Genzel, R., Newman, S., Jones, T., et al. 2011, ApJ, 733, 101
Giavalisco, M., Ferguson, H. C., Koekemoer, A. M., et al. 2004, ApJL, 600, L93
Ginolfi, M., Jones, G. C., Béthermin, M., et al. 2020, A&A, 633, A90
Glenn, J. 2025, AAS Meeting, 245, 216.01
Grogin, N. A., Kocevski, D. D., Faber, S. M., et al. 2011, ApJS, 197, 35
Gutkin, J., Charlot, S., & Bruzual, G. 2016, MNRAS, 462, 1757
Harikane, Y., Ouchi, M., Inoue, A. K., et al. 2020, ApJ, 896, 93
Harikane, Y., Zhang, Y., Nakajima, K., et al. 2023, ApJ, 959, 39
Harish, S., Kartaltepe, J. S., Liu, D., et al. 2025, ApJ, 992, 45
Hashimoto, T., Inoue, A. K., Mawatari, K., et al. 2019, PASJ, 71, 71
Hasinger, G., Capak, P., Salvato, M., et al. 2018, ApJ, 858, 77
Herrera-Camus, R., Bolatto, A. D., Wolfire, M. G., et al. 2015, ApJ, 800, 1
Herrera-Camus, R., Förster Schreiber, N. M., Price, S. H., et al. 2022, A&A, 665, L8
Herrera-Camus, R., González-López, J., Schreiber, N., et al. 2025, A&A, 699, A80
Ikeda, R., Tadaki, K.-i., Mitsuhashi, I., et al. 2025, A&A, 693, A237
Iono, D., Yun, M. S., Elvis, M., et al. 2006, ApJL, 645, L97
Jeong, M.-S., Shapley, A. E., Sanders, R. L., et al. 2020, ApJL, 902, L16
Jones, G. C., Vergani, D., Romano, M., et al. 2021, MNRAS, 507, 3540
Katz, H., Liu, S., Kimm, T., et al. 2022, arXiv:2211.04626
Kauffmann, G., Heckman, T. M., White, S. D. M., et al. 2003, MNRAS, 341, 33
Kennicutt, R. C., Jr. 1998, ApJ, 498, 541
Kewley, L. J., Dopita, M. A., Leitherer, C., et al. 2013, ApJ, 774, 100
Kewley, L. J., Dopita, M. A., Sutherland, R. S., Heisler, C. A., & Trevena, J. 2001, ApJ, 556, 121
Khostovan, A. A., Kartaltepe, J. S., Brinch, M., et al. 2024, arXiv:2411.10537
Khostovan, A. A., Kartaltepe, J. S., Salvato, M., et al. 2025, arXiv:2503.00120
Khusanova, Y., Bethermin, M., Le Fèvre, O., et al. 2021, A&A, 649, A152
Killi, M., Ginolfi, M., Popping, G., et al. 2024, MNRAS, 531, 3222
Klessen, R. S., & Glover, S. C. O. 2023, ARA&A, 61, 65
Koekemoer, A. M., Aussel, H., Calzetti, D., et al. 2007, ApJS, 172, 196
Koekemoer, A. M., Faber, S. M., Ferguson, H. C., et al. 2011, ApJS, 197, 36
Kohandel, M., Pallottini, A., Ferrara, A., et al. 2020, MNRAS, 499, 1250
Kohandel, M., Pallottini, A., Ferrara, A., et al. 2024, A&A, 685, A72
Kormendy, J., & Ho, L. C. 2013, ARA&A, 51, 511
Kriek, M., Shapley, A. E., Reddy, N. A., et al. 2015, ApJS, 218, 15
Le Fèvre, O., Béthermin, M., Faisst, A., et al. 2020, A&A, 643, A1
Le Fèvre, O., Cassata, P., Cucciati, O., et al. 2013, A&A, 559, A14
Lee, L. L., Förster Schreiber, N. M., Herrera-Camus, R., et al. 2025, A&A, 701, A260
Li, J., Da Cunha, E., González-López, J., et al. 2024, ApJ, 976, 70
Lilly, S. J., Carollo, C. M., Pipino, A., Renzini, A., & Peng, Y. 2013, ApJ, 772, 119
Lilly, S. J., Le Fèvre, O., Renzini, A., et al. 2007, ApJS, 172, 70
Lines, N. E. P., Bowler, R. A. A., Adams, N. J., et al. 2025, MNRAS, 539, 2685
Luridiana, V., Morisset, C., & Shaw, R. A. 2015, A&A, 573, A42
Madau, P., & Dickinson, M. 2014, ARA&A, 52, 415
Maiolino, R., Caselli, P., Nagao, T., et al. 2009, A&A, 500, L1
Maiolino, R., Nagao, T., Grazian, A., et al. 2008, A&A, 488, 463
Markov, V., Gallerani, S., Ferrara, A., et al. 2025, NatAs, 9, 458
Marszewski, A., Sun, G., Faucher-Giguère, C.-A., Hayward, C. C., & Feldmann, R. 2024, ApJL, 967, L41
Mazzolari, G., Übler, H., Maiolino, R., et al. 2024, A&A, 691, A345
Mehta, V., Teplitz, H. I., Scarlata, C., et al. 2023, ApJ, 952, 133
Mitsuhashi, I., Tadaki, K.-i., Ikeda, R., et al. 2024, A&A, 690, A197
Momcheva, I. G., Brammer, G. B., van Dokkum, P. G., et al. 2016, ApJS, 225, 27
Morishita, T., Stiavelli, M., Grillo, C., et al. 2024, ApJ, 971, 43
Mowla, L. A., Cutler, S. E., Brammer, G. B., et al. 2022, ApJ, 933, 129
Mowla, L. A., van Dokkum, P., Brammer, G. B., et al. 2019, ApJ, 880, 57
Muñoz-Elgueta, N., Arrigoni Battaia, F., Kauffmann, G., et al. 2024, A&A, 690, A392
Nagao, T., Maiolino, R., & Marconi, A. 2006, A&A, 459, 85
Nakajima, K., & Maiolino, R. 2022, MNRAS, 513, 5134
Nakajima, K., Ouchi, M., Isobe, Y., et al. 2023, ApJS, 269, 33
Navarro-Carrera, R., Rinaldi, P., Caputi, K. I., et al. 2024, arXiv:2410.23249
Nebrin, O. 2023, RNAAS, 7, 90
Newman, S. F., Genzel, R., Förster-Schreiber, N. M., et al. 2012, ApJ, 761, 43
Noeske, K. G., Weiner, B. J., Faber, S. M., et al. 2007, ApJL, 660, L43
Oke, J. B. 1974, ApJS, 27, 21
Osterbrock, D. E., & Ferland, G. J. 2006, Astrophysics of Gaseous Nebulae and Active Galactic Nuclei (Sausalito, CA: Univ. Science Books)
Pallottini, A., Ferrara, A., Gallerani, S., et al. 2025, A&A, 699, 6
Pérez-Montero, E., Hägele, G. F., Contini, T., & Díaz, Á. I. 2007, MNRAS, 381, 125
Pirzkal, N., Finkelstein, S., Papovich, C. & Ngdeep Team 2023, AAS Meeting, 241, 455.04

Pizzati, E., Ferrara, A., Pallottini, A., et al. 2020, MNRAS, 495, 160
Pizzati, E., Ferrara, A., Pallottini, A., et al. 2023, MNRAS, 519, 4608
Pontoppidan, K. M., Pickering, T. E., Laidler, V. G., et al. 2016, Proc. SPIE, 9910, 991016
Popping, G., Somerville, R. S., & Galametz, M. 2017, MNRAS, 471, 3152
Posses, A., Aravena, M., González-López, J., et al. 2025, A&A, 699, 256
Reddy, N. A., Kriek, M., Shapley, A. E., et al. 2015, ApJ, 806, 259
Reddy, N. A., Shapley, A. E., Sanders, R. L., et al. 2025, arXiv:2506.17396
Ren, W., Silverman, J., Faisst, A. L., et al. 2025, MNRAS, 544, 211
Riechers, D. A., Carilli, C. L., Capak, P. L., et al. 2014, ApJ, 796, 84
Rigby, J., Perrin, M., McElwain, M., et al. 2023, PASP, 135, 048001
Robertson, B. E. 2022, ARA&A, 60, 121
Romano, M., Cassata, P., Morselli, L., et al. 2021, A&A, 653, A111
Romano, M., Donevski, D., Junais, et al. 2024, A&A, 683, L9
Rowland, L. E., Stefanon, M., & Bouwens, R. 2025, arXiv:2501.10559
Rudie, G. C., Steidel, C. C., Trainor, R. F., et al. 2012, ApJ, 750, 67
Salim, S., & Narayanan, D. 2020, ARA&A, 58, 529
Sanders, R. L., Shapley, A. E., Jones, T., et al. 2021, ApJ, 914, 19
Sanders, R. L., Shapley, A. E., Topping, M. W., Reddy, N. A., & Brammer, G. B. 2024, ApJ, 962, 24
Sarkar, A., Chakraborty, P., Vogelsberger, M., et al. 2025, ApJ, 978, 136
Scarlata, C., Hayes, M., Panagia, N., et al. 2024, arXiv:2404.09015
Schaerer, D., Ginolfi, M., Béthermin, M., et al. 2020, A&A, 643, A3
Schimek, A., Decataldo, D., Shen, S., et al. 2024, A&A, 682, A98
Scholtz, J., Maiolino, R., D'Eugenio, F., et al. 2025, A&A, 697, A175
Scoville, N., Aussel, H., Brusa, M., et al. 2007, ApJS, 172, 1
Shapley, A. E., Sanders, R. L., Reddy, N. A., Topping, M. W., & Brammer, G. B. 2023, ApJ, 954, 157
Shapley, A. E., Sanders, R. L., Reddy, N. A., et al. 2017, ApJL, 846, L30
Shapley, A. E., Sanders, R. L., Salim, S., et al. 2022, ApJ, 926, 145
Shapley, A. E., Sanders, R. L., Topping, M. W., et al. 2025, ApJ, 980, 242
Shi, F., Zhao, G., & Liang, Y. C. 2007, A&A, 475, 409
Shim, H., Chary, R.-R., Dickinson, M., et al. 2011, ApJ, 738, 69
Shuntov, M., Akins, H. B., Paquereau, L., et al. 2025, arXiv:2506.03243
Solimano, M., González–López, J., Aravena, M., et al. 2025, A&A, 693, A70
Sommovigo, L., Ferrara, A., Carniani, S., et al. 2022, MNRAS, 517, 5930
Stark, D. P., Schenker, M. A., Ellis, R., et al. 2013, ApJ, 763, 129
Steidel, C. C., Rudie, G. C., Strom, A. L., et al. 2014, ApJ, 795, 165
Steinhardt, C. L., Speagle, J. S., Capak, P., et al. 2014, ApJL, 791, L25
Storey, P. J., & Hummer, D. G. 1995, MNRAS, 272, 41
Stott, J. P., Swinbank, A. M., Johnson, H. L., et al. 2016, MNRAS, 457, 1888
Strom, A. L., Rudie, G. C., Trainor, R. F., et al. 2023, ApJL, 958, L11
Strom, A. L., Steidel, C. C., Rudie, G. C., et al. 2017, ApJ, 836, 164
Sun, G., Muñoz, J. B., Mirocha, J., & Faucher-Giguère, C.-A. 2025, JCAP, 2025, 034
Swinbank, A. M., Sobral, D., Smail, I., et al. 2012, MNRAS, 426, 935
Tacconi, L. J., Genzel, R., & Sternberg, A. 2020, ARA&A, 58, 157
Telikova, K., González-López, J., Aravena, M., et al. 2025, A&A, 699, 5
Triani, D. P., Sinha, M., Croton, D. J., Dwek, E., & Pacifici, C. 2021, MNRAS, 503, 1005
Tsujita, A., Fujimoto, S., Faisst, A., et al. 2025, arXiv:2510.18248
Vanderhoof, B. N., Faisst, A. L., Shen, L., et al. 2022, MNRAS, 511, 1303
Veraldi, E., Vallini, L., Pozzi, F., et al. 2025, A&A, 693, A34
Vijayan, A. P., Clay, S. J., Thomas, P. A., et al. 2019, MNRAS, 489, 4072
Volonteri, M., Habouzit, M., & Colpi, M. 2021, NatRP, 3, 732
Weaver, J. R., Kauffmann, O. B., Ilbert, O., et al. 2022, ApJS, 258, 11
Welch, B., Rigby, J. R., & Hutchison, T. A. 2023, RNAAS, 7, 17
Wisnioski, E., Förster Schreiber, N. M., Fossati, M., et al. 2019, ApJ, 886, 124
Wisnioski, E., Mendel, J. T., Leaman, R., et al. 2025, MNRAS, in press
Wong, Y. H. V., Wang, P., Hashimoto, T., et al. 2022, ApJ, 929, 161
Yang, H., Malhotra, S., Rhoads, J. E., & Wang, J. 2017, ApJ, 847, 38
Zavala, J. A., Castellano, M., Akins, H. B., et al. 2025, NatAs, 9, 155
Ziparo, F., Ferrara, A., Sommovigo, L., & Kohandel, M. 2023, MNRAS, 520, 2445